PREDICTABILITY OF THE ATMOSPHERE AND OCEANS: FROM DAYS TO DECADES

T.N.PALMER
ECMWF
Shinfield Park
Reading, RG2 9AX, UK
tim.palmer@ecmwf.int

Contents

1 Introduction

This paper is concerned with the predictability of the atmosphere and oceans on timescales of days to decades. A variety of phenomena will be discussed, from individual weather events through weather regimes and El Niño, to decadal ocean-atmosphere fluctuations and climate change. However, no matter what timescale or phenomenon is being considered, we shall be studying processes which are believed to be fundamentally chaotic.

A chaotic system can be defined as one whose evolution is sensitive to initial conditions. However, this is not to say that the unpredictability associated with this sensitivity is only of importance for initial-value problems. For example, determining the impact on climate of doubling CO_2 is not primarily an initial value problem. Nevertheless, the fact that the climate is chaotic has fundamental implications for the predictability of this type of question. Just as initial conditions for a weather forecast are not perfectly accurate, and hence can only be specified completely in terms of some probability distribution, so also the formulation of a climate model (associated with the physical parametrisations in particular) is only approximate, and again can only be specifed completely in terms of some stochastic distribution. The instabilities that amplify uncertainties in the initial state, may also amplify uncertainties in model formulation.

We start in section 2 with a discussion on predictability of initial value problems. As suggested above, a fundamental quantity in this discussion is the forecast probability density function (PDF). The evolution of this PDF can be described in the first phase of the forecast by linearised dynamics. The semi-major axes of the PDF are given by the dominant singular vectors of the linear evolution operator (using the so- called Mahalanobis inner product). We relate these singular vectors to more familiar quantities associated with eigenmode growth on the one hand, and to Lyapunov exponent growth on the other. We also discuss the relationship of singular vectors and so-called breeding vectors.

In section 3, we apply the methodology developed in section 2 to study predictability associated with a variety of phenomena on timescales ranging from days to seasons. In particular, the singular vector instability of individual extratropical weather systems, and of the coupled ocean-atmosphere El Niño/Southern Oscillation, is studied. For example, we demonstate the endemic upscale energy cascade associated with extratropical predictability, and indicate that this effect is much less predominant in the tropics. In doing this a new interpretation of the Charney-Shukla paradigm for large-scale tropical predictability is given.

In section 4, we discuss the predictability of forced problems (predictability of the second kind). Explicit examples are given using both the Lorenz 3-component model, and the global circulation models (GCMs). We develop a basic nonlinear paradigm for analysing the response to an external perturbation. The basic notion is that the influence of a weak external forcing is greatest in regions of phase space where the system is particularly unstable; however, the response of the system is greatest in regions of phase space where the system is particlarly stable. The extratropical response of the atmosphere to extratropical sea surface temperature (SST) anomalies is discussed using this paradigm.

In section 5, the predictability of natural fluctuations of the climate system on decadal timescales is discussed on the basis of a number of GCM integrations. One fundamental question concerns the relative contribution of the atmospheric and oceanic dyamics in contributing to observed decadal variability. It is found that, even on decadal timescales, the role of purely internal atmospheric variability is not negligible. This itself implies that the predictability of decadal fluctuations may not be strong. However, in addition, it is suggested that the role of the extratropical oceans is basically to redden the spectrum

of atmospheric variability, *eg* by increasing the typical residence time of the atmospheric state vector within a weather regime. As such, decadal atmospheric variability linked directly to decadal SST variability may not itself be strongly predictable.

In section 6, the nonlinear paradigm discussed earlier is applied to the problem of climate change. We assess whether or not the observed warming of the atmosphere can be attributed to the greenhouse effect. It is suggested that the observed warming over the past few decades can be largely interpreted in terms of an increase in the frequency of one of the dominant regimes of the extratropical flow. Singular vector analysis suggests that this regime may be most sensitive to forcing in the tropical west Pacific warm pool region. This therefore may be the most critical area for understanding how enhanced CO_2 may influence global climate. The predictability implications of this analysis are discussed.

In section 7, some remarks are made about the rationalisation of climate and weather prediction models.

In this paper, we shall make some use of low-dimensional chaotic models. This does not imply that I think that the climate necessarily has a low-dimensional attractor. Rather, for some purposes, I believe the use of relatively simple models can be helpful to illustrate basic processes. On the other hand, as (singular vector) calculations in the body of the text suggest, there are other circumstances where comparison with a turbulent fluid may be more appropriate.

2 PREDICTABILITY OF THE FIRST KIND

2.1 The forecast probability density function

As mentioned in the introduction, we can distinguish two basic types of prediction. Following Lorenz (1975), predictions of the first kind are initial value problems (*eg* medium-range weather forecasts with an atmosphere model, or seasonal forecasts with a coupled ocean-atmosphere model). Predictability of the first kind is therefore concerned with the question of how uncertainties in the initial state evolve during the forecast and limit its skill.

The predictability of a system is strongly dependent on its stability properties. If the system is particularly unstable, then any uncertainty in the initial state that projects significantly onto one of these instabilities will severely limit the skill of an initial-value forecast. Let us try to be more precise. Suppose we represent the uncertainty in the initial condition for a prediction of the first kind in terms of a PDF in some finite m-dimensional phase space. For example, for each direction in phase space, let us assume this PDF to be normally distributed about our best estimate of the initial state. The standard deviation of this normal distribution will, in general, vary with direction. However, we can define a metric on the phase space (local to the initial condition) so that the standard deviations are independent of direction (see section 2.7 for a more explicit description of this). With respect to this metric, the PDF will now be isotropic, and isopleths of the PDF will bound an m-dimensional ball (see Fig 2.1a).

A quantitative measure of predictability can be defined in relation to the properties of the evolution of this initial PDF. In the early part of the forecast, error growth is governed by linear dynamics. During this period, initially spherical isopleths of the PDF will evolve to bound an m-dimensional ellipsoidal volume (see Fig 2.1b). The major axis of the ellipsoid corresponds to a phase-space direction which defines the dominant instability of that part of phase space. The ratio of the standard deviation of the PDF along this major axis, compared with the initial standard deviation, is a measure of the amplification

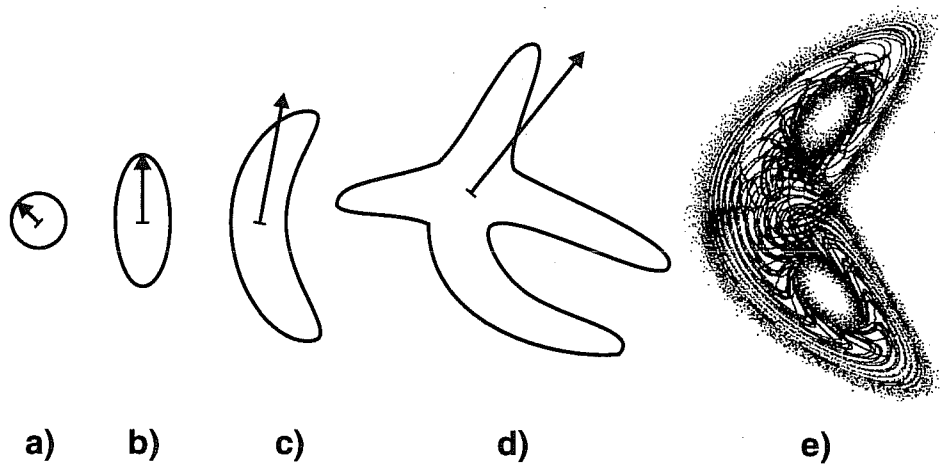

Figure 2.1: Schematic evolution of the probability density function (PDF) of forecast error. Initially (a) the analysis error distribution is isotropic (with respect to the appropriate Mahalanobis metric). During the linear stage of evolution (b), the error ball evolves into an ellipsoid. A vector pointing along the major axis is shown in (b), and its pre-image at initial time is shown in (a). The weakly nonlinear stage of evolution is shown in (c). During this phase, there is significant agreement between the evolution of the vector in (b) and the principal direction in which the distance of an isopleth of probability from the mode of the distribution is maximal. In the strongly nonlinear stage of evolution (d), the relationship between the PDF and the evolved directions of the major axes of the linear ellipsoid breaks down. Total loss of predictability (e) occurs when the PDF essentially covers the attractor.

rate associated with this dominant instability (and indeed is a measure of the l^∞ norm of the operator which maps initial perturbations to forecast perturbations). In addition to this major axis direction, there may be other orthogonal directions in which the initial PDF has amplified significantly; these clearly define secondary directions of instability.

Before giving a quantitative description of this linear stage, we show (schematically) three further stages in the evolution of the forecast PDF. The growth of the PDF between Fig 2.1b and Fig 2.1c could be described as 'weakly nonlinear'. In Fig 2.1c the PDF has deformed from its ellipsoidal shape in Fig 2.1b. From the centroid of this PDF, one can define directions D_i for which the distance from the centroid to a chosen isopleth of the PDF is maximised. During the weakly nonlinear period, the evolution of the major axis directions E_i, from Fig 2.1b to Fig 2.1c will be close to the directions D_i.

The growth of the PDF after Fig 2.1c can be described as 'strongly nonlinear'. In particular, for the PDF in Fig 2.1d, there may be no correspondence between the dominant directions D_i (defined as above) and the directions corresponding to evolution of the major axis directions in Fig 2.1b. For example, it might be that one of the dominant directions shown in Fig 2.1d arose from the evolution of a minor axis direction in Fig 2.1b. Although the evolution of the PDF is strongly nonlinear, predictability has not necessarily been lost at the stage corresponding to Fig 2.1d. Rather, predictability is lost when the PDF isopleth has evolved to cover the entire attractor (*cf* Fig 2.1e).

It should be noted that the timescales associated with the 'linear', 'weakly nonlinear' and 'strongly nonlinear' phases of evolution depend on which isopleth of the PDF one is considering. An isopleth of small probability will bound a larger volume at initial time than an isopleth of large probability. Consequently, the timescales will be shorter for the small-probability isopleth. In practice, for numerical weather prediction, there is evidence that errors of about one standard deviation of the analysis error PDF evolve linearly for

2-3 days, and that the 'weakly nonlinear' phase lasts until about day 7 of the forecast (see section 3.3).

2.2 Singular Vectors

Let us try to quantify further the linear stage of evolution of the forecast PDF between Fig 2.1a and Fig 2.1b. Let us suppose our basic system is described by the (m-dimensional) nonlinear evolution equation

$$\frac{d\mathbf{X}}{dt} = \mathbf{M}[\mathbf{X}] \tag{2.1}$$

Consider a small perturbation $\mathbf{x}$ of the state vector $\mathbf{X}$. For sufficiently short time intervals, its evolution can be described by the linearised approximation

$$\frac{d\mathbf{x}}{dt} = \mathbf{M}_l\mathbf{x} \tag{2.2}$$

of (2.1). $\mathbf{M}_l \equiv \frac{d\mathbf{M}}{d\mathbf{X}} \mid_{\mathbf{X}(t)}$ is the linear evolution operator evaluated on the nonlinear trajectory $\mathbf{X}(t)$.

Equation (2.2) can be written in the integral form

$$\mathbf{x}(t) = \mathbf{L}(t, t_0)\mathbf{x}(t_0) \tag{2.3}$$

In practice, we estimate $\mathbf{L}$ in (2.3) by splitting up the trajectory into many short quasi-stationary segments. For each segment we can write

$$\mathbf{L}(t_i, t_j) = e^{(t_i - t_j)\mathbf{M}_l} \tag{2.4}$$

(Because the full trajectory segment is time-varying, we cannot, in general, write $\mathbf{L}(t, t_0)$ in terms of the operator exponential.)

The operator $\mathbf{L}(t, t_0)$ is referred to as the forward tangent propagator; it maps small perturbations along the (nonlinear) trajectory from an initial time t_0 to some future time t. For the application to weather prediction, if $\mathbf{x}(t_0)$ is the typical error in the initial conditions for a weather forecast, then (2.2) and (2.3) hold for approximately 2-3 days of integration time.

We now define an inner product $(\mathbf{x}; \mathbf{y})$, which in turn defines a metric on the tangent space. Following the discussion above this inner product is not arbitrary, it is defined so that the PDF of the initial conditions is isotropic. As discussed in section 2.7, the atmospheric PDF appears reasonably isotropic using an inner product based on total perturbation energy. Using (2.3), the perturbation norm at time t is given by

$$\|\mathbf{x}(t)\|^2 \equiv (\mathbf{x}(t); \mathbf{x}(t)) = (\mathbf{x}(t_0); \mathbf{L}^*\mathbf{L}\mathbf{x}(t_0)) \tag{2.5}$$

where $\mathbf{L}^*$ is the adjoint of $\mathbf{L}$ with respect to the energy inner product. Note that if $\mathbf{L}$ is represented in matrix form, then $\mathbf{L}^*$ is just the matrix transpose of $\mathbf{L}$.

Unlike $\mathbf{L}$ itself, the operator $\mathbf{L}^*\mathbf{L}$ (sometimes referred to as the Oseledec operator, *eg* Abarbanel *et al*, 1991) is easily shown to be symmetric. Hence its eigenvectors $\boldsymbol{\nu}_i(t_0)$ can be chosen to form an orthonormal basis (assumed complete) in the m-dimensional tangent space of linear perturbations, with real eigenvalues $\sigma_i^2 \geq 0$ (*eg* Noble and Daniel, 1977) *i.e.*

$$(\mathbf{L}^*\mathbf{L})\boldsymbol{\nu}_i(t_0) = \sigma_i^2\boldsymbol{\nu}_i(t_0) \tag{2.6}$$

At future time t, these eigenvectors evolve to $\boldsymbol{\nu}_i(t) = \mathbf{L}\boldsymbol{\nu}_i(t_0)$ which in turn satisfy the eigenvector equation

$$(\mathbf{L}\mathbf{L}^*)\boldsymbol{\nu}_i(t) = \sigma_i^2\boldsymbol{\nu}_i(t) \tag{2.7}$$

From eqs. (2.5) and (2.6),

$$||\boldsymbol{\nu}_i(t)||^2 = (\boldsymbol{\nu}_i(t_0); \mathbf{L}^*\mathbf{L}\boldsymbol{\nu}_i(t_0)) = \sigma_i^2 \tag{2.8}$$

Since, by completeness, any $\mathbf{x}(t)/||\mathbf{x}(t_0)||$ can be written as a linear combination of the set $\boldsymbol{\nu}_i(t)$, it follows that

$$max_{\mathbf{x}(t_0)\neq 0}\left(\frac{||\mathbf{x}(t)||}{||\mathbf{x}(t_0)||}\right) = \sigma_1 \tag{2.9}$$

Following the terminology of linear algebra, the σ_i, ranked in terms of magnitude, are called the singular values of the operator $\mathbf{L}$ and the vectors $\boldsymbol{\nu}_i(t)$ are called the singular vectors of $\mathbf{L}$. Maximum energy growth over the time interval $t - t_0$ is therefore associated with the dominant singular vector: $\boldsymbol{\nu}_1(t_0)$ at initial time, and $\boldsymbol{\nu}_1(t)$ at optimisation time. Following the discussion above, the $\boldsymbol{\nu}_i(t)$ define the directions of the axes of the forecast PDF ellipsoid, with $\boldsymbol{\nu}_1(t)$ defining the major axis, $\boldsymbol{\nu}_2(t)$ the second major axis, and so on. The directions at initial time that evolve into these axes are given by $\boldsymbol{\nu}_1(t_0), \boldsymbol{\nu}_2(t_0)$ respectively. The amplification of the PDF standard deviations associated with these directions are given by the σ_i.

As far as I am aware, a discussion of singular vector growth in meteorology was first given by Lorenz (1965).

2.3 Correspondence with 'Normal' Mode Instability

Singular vector analysis is in some sense a generalisation of classical normal mode instability analysis. This can be made explicit by linearising about a stationary solution of (2.1), so that normalised eigenvectors $\boldsymbol{\xi}_i$ of $\mathbf{M}_l$ with eigenvalues μ_i give rise to modal solutions $\boldsymbol{\xi}_i e^{\mu_i(t-t_0)}$ of (2.2). The integral operator $\mathbf{L}(t, t_0)$ can be written as $e^{(t-t_0)\mathbf{M}_l}$, with eigenvectors $\boldsymbol{\xi}_i$ and eigenvalues $e^{(t-t_0)\mu_i}$.

For application to atmosphere-ocean dynamics, the linear evolution operators associated with realistic basic state flows are never normal (*ie* $\mathbf{L}^*\mathbf{L} \neq \mathbf{L}\mathbf{L}^*$) because of vertical and horizontal shear (*eg* Farrell and Ioannou, 1996). Now, it is common meteorological parlance to call any modal eigenvectors as 'normal' modes. However, for any meteorological basic state these eigenvectors are not eigenvectors of a normal operator (and hence not normal). In future we refer to such eigenvectors as 'eigenmodes' (hence the quotation marks in the title of this sub-section). However, irrespective of normality, eigenvectors $\boldsymbol{\eta}_i$ and eigenvalues θ_i of the adjoint operator $\mathbf{L}^*$ satisfy the biorthogonality condition

$$(\mu_i - \theta_i^{cc})(\boldsymbol{\eta}_i; \boldsymbol{\xi}_i) = 0 \tag{2.10}$$

where 'cc' denotes complex conjugate. This condition ensures that the eigenvalues of an eigenvector/adjoint eigenvector pair that are not orthogonal, must form a complex conjugate pair. The magnitude of the inner product $(\boldsymbol{\eta}_i; \boldsymbol{\xi}_i)$ for such eigenvector pairs equals the cosine of the angle, α_i, they subtend in phase space.

If an initial disturbance comprises a linear combination of the eigenmodes $\boldsymbol{\xi}_i$ so that

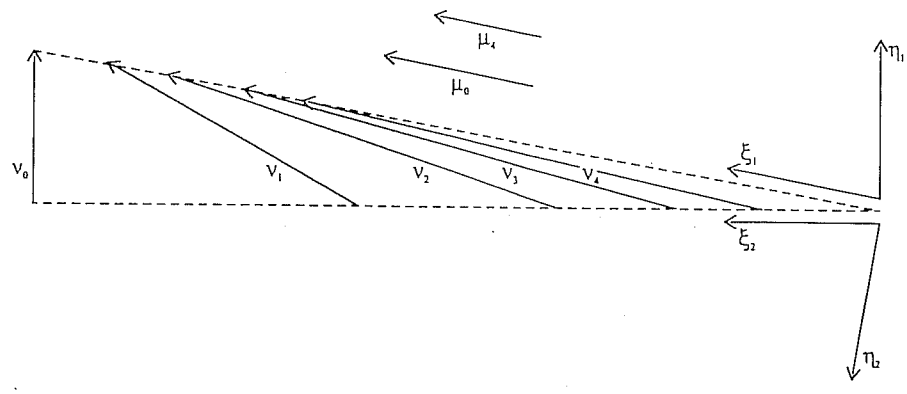

Figure 2.2: This diagram illustrates schematically the crucial difference between eigenmode and singular vector growth, and the relationship between singular vectors and adjoint modes. See text for details.

$$\mathbf{x}(t) = \sum_i c_i \boldsymbol{\xi}_i e^{\mu_i (t-t_0)} \tag{2.11}$$

then from the biorthogonality condition (2.10)

$$c_i = (\boldsymbol{\eta}_i; \mathbf{x}(t_0))/(\boldsymbol{\eta}_i; \boldsymbol{\xi}_i) \tag{2.12}$$

From (2.11), the fastest growing eigenmode will ultimately dominate the linear combination. Hence for sufficiently long optimisation times, the dominant singular vector at optimisation time will correspond to the most unstable eigenmode. (Since the singular values are real, whilst the eigenvalues are complex, there is an arbitrary phase factor that has to be defined to make this correspondence precise.)

In order to maximise the contribution of the first eigenmode at optimisation time, c_1 in (2.11) should be as large as possible. If $\mathbf{x}(t_0)$ equals $\boldsymbol{\xi}_1$ then from (2.12), $c_1 = 1$ which could be highly sub-optimal. In fact, if $\mathbf{x}(t_0)$ projects onto $\boldsymbol{\eta}_1$, then c_1 is maximised and is given by the projectibility factor $1/(\cos\alpha_1)$ (Zhang, 1988).

Hence, for indefinitely long optimisation time, the dominant singular vector, at initial time, is determined by the first adjoint eigenmode, whilst the dominant singular vector at optimisation time is determined by the first eigenmode itself. The singular value will depend on both the e-folding time of the dominant eigenmode and its projectibility. For finite optimisation time, the dominant singular vectors will no longer project onto individual eigenmode solutions (and their adjoints), and the amplitude of finite-time instabilities need not be bounded by properties of the dominant eigenmodes alone.

Fig 2.2 illustrates schematically the crucial difference between eigenmode and singular vector growth, and the relationship between singular vectors and adjoint modes. An idealised 2-D system has two very non-orthogonal decaying eigenmodes $\boldsymbol{\xi}_1$ and $\boldsymbol{\xi}_2$. We take $\boldsymbol{\xi}_1$ to have the larger real eigenvalue component. The adjoint eigenmodes $\boldsymbol{\eta}_1$ and $\boldsymbol{\eta}_2$ are shown with $\boldsymbol{\eta}_1$,$\boldsymbol{\eta}_2$ orthogonal to $\boldsymbol{\xi}_2$,$\boldsymbol{\xi}_1$ respectively (according to the biorthogonality condition 2.10). A normalised vector $\boldsymbol{\nu}_0$ is shown parallel to $\boldsymbol{\eta}_1$. Its time evolution can be estimated by mapping the tip and tail of $\boldsymbol{\nu}_0$ along the $\boldsymbol{\xi}_1$ and $\boldsymbol{\xi}_2$ directions (shown as dashed lines) using the modal decay rates. The sequence of vectors $\boldsymbol{\nu}_n$, $n = 1, 2, \ldots$ giving the time evolution of $\boldsymbol{\nu}_0$ increases in amplitude up to some finite $n = N$ and is aligned almost entirely with $\boldsymbol{\xi}_1$ for large n. The projection of $\boldsymbol{\nu}_n$ onto $\boldsymbol{\xi}_1$ for large n is much larger than that associated with the evolution of a second normalised vector μ_n which is initially

aligned along $\boldsymbol{\xi}_1$. The sequence $\boldsymbol{\nu}_n$, $n = 1, 2, ...$ describes singular vector growth over a long time interval. The transient growth of the singular vectors in such systems was first noted by Orr (1907), and a review of this process in plane parallel shear flow (and its relationship to wave overreflection) is discussed in Lindzen (1988).

2.4 Correspondence with Lyapunov Exponent Growth

If, instead of linearising about a stationary flow, let us consider the other extreme of linearising about a (time-evolving) trajectory portion which is sufficiently long to approximately cover the entire climate attractor.

Specifically, if we apply the forward tangent propagator N times from t_0 so that

$$\mathbf{x}(t_n) = \mathbf{L}(t_n, t_{n-1})\mathbf{x}(t_{n-1}) \tag{2.13}$$

with $t_n - t_{n-1} = \Delta t$ a unit time interval, then according to the Multiplicative Ergodic theorem of Oseledec (1968), the eigenvalues of the Oseledec matrix

$$[\mathbf{L}(t_n, t_0), \mathbf{L}(t_n, t_0)]^{\frac{1}{2n}} \tag{2.14}$$

are independent of initial conditions as $n \rightarrow \infty$, and hence are invariants of the dynamical system. The logarithms of these eigenvalues are the Lyapunov exponents l_i.

It is straightforward to see that the singular values σ_i of the propagator $\mathbf{L}(t_n, t_0)$ are related to the Lyapunov exponents by the equation

$$l_i = lim_{n\rightarrow\infty}[\frac{1}{n}\ln\sigma_i] \tag{2.15}$$

From this, some authors (*eg* Abarbanel *et al*, 1991) define the local Lyapunov exponents $l_i(t_1, t_0)$ of the attractor between t_1 and t_0 as

$$l_i(t_1, t_0) = \frac{1}{t_1 - t_0}\ln\sigma_i(t_1, t_0) \tag{2.16}$$

The corresponding singular vectors can therefore be referred to as local Lyapunov vectors, although it should be noted that this terminology is not universal (*eg* Toth and Kalnay, 1996).

2.5 Projection Operators

Singular vectors are, in general, not modal. For the application in section 3.2, their shapes evolve not only in geographical space but also in their spectral distribution of energy. As we shall see for extratropical weather systems, this spectral evolution describes, in a linear context, the upscale energy transfer associated with turbulent processes. In order to study this upscale energy transfer more explicitly we introduce a spectral projection operator $\mathbf{P}_{[n_1,n_2]}$ where $[n_1, n_2]$ denotes the total wavenumber interval $n_1 \leq n \leq n_2$. $\mathbf{P}_{[n_1,n_2]}$ is defined as

$$\begin{aligned} \mathbf{P}_{[n_1,n_2]}\mathbf{x}_n &= \mathbf{x}_n \text{ if } n\epsilon[n_1, n_2] \\ \mathbf{P}_{[n_1,n_2]}\mathbf{x}_n &= 0 \text{ otherwise} \end{aligned} \tag{2.17}$$

Here $\mathbf{x}_n$ is the wavenumber n component of the spherical harmonic expansion of the (atmospheric) state vector. If we wish to find perturbations, initially constrained to be

in $[n_3, n_4]$, with maximum energy in $[n_1, n_2]$, these are given by the singular vectors of $\mathbf{P}_{[n_1,n_2]}\mathbf{L}\mathbf{P}_{[n_3,n_4]}$. A similar projection operator can be applied to study singular vectors whose energy is optimised to a specific geographical area (for applications, see Buizza and Palmer, 1995; Hartmann *et al*, 1995).

2.6 Numerical Solution

When systems with a large number of degrees of freedom (*eg* $0(10^4)$ or more) are considered, the eigenvalue problem (2.6, 2.7) cannot be solved using direct methods. However, iterative techniques provide an alternative possibility if the adjoint propagator has been coded. The power method, whereby a random initial vector is operated on repeatedly by $\mathbf{L}^*\mathbf{L}$, is an example. A more sophisticated technique such as the Lanczos algorithm (Strang, 1986) is required if more than the largest singular vector is required. More recently, calculations with the Jacobi-Davidson method (Sleijpen and van der Vorst, 1995) has proved both efficient, and allowed estimation of generalised eigenvectors (see section 2.7 below).

2.7 Singular Vectors and Eigenvectors of the Forecast and Analysis Error Covariance Operator.

We discussed above the notion that there is a natural inner product defined such that the PDF of the initial state is isotropic with respect to this metric. In this section we shall show this more explicitly, and give evidence that the total energy is a reasonable approximation to this preferred inner product.

Consider an initial state of an operational weather forecast, determined by the operational data assimilation system. We can think of this initial state as a point X in the phase space of the numerical weather prediction model. Now, as mentioned, a complete operational data assimilation system should be able to determine not only the initial state, but also an estimate of the probability that the initial state is in error by a given amount.

To make this idea more precise, let us consider the (linear) vector space T_X tangent to X, and let $d\mu$ denote the probability that the error lies in a small volume at the point $e^i \epsilon T_X$ (*ie* μ is a measure on T_X). Here we shall use some elementary tensor algebra, with the convention that repeated indices imply summation. Let us assume that the operational analysis is our best unbiased estimate of truth, so that at initial time

$$m^i = \int e^i d\mu = 0 \tag{2.18}$$

The covariance of analysis error associated with this measure is given by the contravariant second-rank tensor

$$C^{ij} = \int e^i e^j d\mu \tag{2.19}$$

The linear transformation (2.3) between $T_{X(t_0)}$ and $T_{X(t)}$ can be written (in index form) as

$$\hat{e}^i = L^i{}_j e^j \tag{2.20}$$

which takes analysis errors e^j to forecast errors $\hat{e}^i$. In terms of this linear mapping, the covariance matrix is transformed as a second rank tensor to the forecast covariance

$$\hat{C}^{kl} = L^k{}_i L^l{}_j C^{ij} \tag{2.21}$$

Now we are going to define a metric g_{ij} which defines the (scalar) inner product

$$s = g_{ij} x^i y^j \tag{2.22}$$

between any two vectors x^i and y^j. There are many choices of inner product possible; however, we shall single one out as being special. It is the metric in which the analysis error covariance tensor is isotropic, *ie* is defined so that

$$C^{ij} g_{jk} = \delta^i{}_k \tag{2.23}$$

the right hand side being the Kronecker delta. This can be written equivalently as

$$C^{ij} = g^{ij} \tag{2.24}$$

where

$$g^{ij} g_{jk} = \delta^i{}_k \tag{2.25}$$

defines the inverse or contravariant metric.

With this choice of metric, the forecast error covariance operator can be written

$$\hat{C}^k{}_l = L^k{}_i L_l{}^i \tag{2.26}$$

Equation (2.26) can be expressed in matrix form

$$\hat{\mathbf{C}} = \mathbf{L}\mathbf{L}^* \tag{2.27}$$

where

$$L^{*i}{}_j = L_j{}^i \tag{2.28}$$

is the adjoint propagator. Hence with the specific choice of metric (2.24), the eigenvectors of $\hat{\mathbf{C}}$ are precisely the evolved singular vectors of $\mathbf{L}$. The vectors at initial time which evolve into these directions at the forecast time are given by the corresponding initial singular vectors of $\mathbf{L}$. This choice of metric is sometimes known as the Mahalanobis metric (*eg* Mardia *et al*, 1979).

How do we define a metric in practice? Three simple choices are based on the enstrophy, energy and streamfunction squared. The spherical harmonic spectrum of typical 48-hour enstrophy and energy-norm singular vectors are shown in Fig 2.3 at initial (dashed) and at final (solid) time. The enstrophy spectrum (Fig 2.3a) of the enstrophy SVs are red at initial time, blue at final time. Because of the large enstrophy amplification, values at initial time are multiplied by 40 to plot them on the same scale as final values. (However, Fig 2.3b, which has no rescaling, shows that there is little energy amplification associated with these enstrophy SVs.) By contrast, the energy spectrum (Fig 2.3c) of the energy SVs peaks at sub-synoptic scales at initial time and at synoptic scales at optimisation time.

We now want to compare these spectra with spectra of analysis error. As a surrogate for a set of analysis error fields, let us take the differences between analyses made during periods when the ECMWF operational system and some (potentially operational) experimental system were being run in parallel. We have chosen two different periods when such

parallel tests were being made. The first corresponded to the testing of an experimental model formulation, the second to the testing of an experimental analysis methodology (3-dimensional variational data assimilation, 3DVAR). Twenty one analysis difference fields were taken from each period. The total horizontal wavenumber spectra of the energy, enstrophy, and streamfunction squared difference fields associated with the northern extratropical component of these difference fields are shown in Fig 2.4a-c respectively. It is clear that in terms of energy, the difference field is indeed almost white. By contrast, the enstrophy spectrum is blue and the streamfunction squared spectrum is red. (Molteni *et al*, 1996, have demonstrated that these results can be replicated using difference fields from operational analyses from different operational centres.) Comparing 2.4 with 2.3 we can rule out enstrophy as a suitable metric (the initial enstrophy singular vectors have no amplitude on small scales, whilst the analysis errors have all their enstrophy on small scales). A streamfunction metric would also be ruled out (although not shown, an initial streamfunction singular vector is strongly peaked at high wavenumbers). Only the energy metric shows some consistency between singular vector and analysis error structure.

A more accurate estimate of inner product is, in principle, available from the 3DVAR data assimilation system. In 3DVAR a cost function J based on both data and a first guess error, is minimised. The second derivative, or Hessian, of the cost function gives a measure of the analysis error covariance. In terms of the Hessian, the singular vector computation becomes equivalent to a generalised eigenvector problem. In 3DVAR the Hessian is known in operator form (Fisher and Courtier, 1995). Tests are in progress, using the Jacobi-Davidson scheme, to estimate the corresponding singular vectors using this Hessian. Further generalisation, in which the background error covariance in the Hessian is flow dependent, will be possible with the development of Kalman filter schemes (Bouttier, 1993).

2.8 Correspondence with breeding vectors

Toth and Kalnay (1993, 1995) have discussed a technique which they use to generate initial perturbations for the NMC model. The technique is referred to as 'breeding', and is simply described. A random initial perturbation is generated with a specified amplitude, characteristic of a typical uncertainty in the initial state. Two integrations are run over a specified cycle time (*eg* 12 hours). The first is an integration of the operational weather prediction model from the operational initial state. The second integration is made using the same model, but is initialised by adding the perturbation to the operational analysis. At the end of the integration period, the difference between the two integrations is renormalised using the specified amplitude. The process is repeated for the next cycle time using the renormalised perturbation to generate the perturbed initial state.. The process is repeated ad infinitum. Toth and Kalnay (1995) call the breeding vectors, local Lyapunov vectors. Clearly they are not entirely local, depending on the history of evolution of the breeding vector. A more accurate description would be in terms of the local orientation of the global Lyapunov vectors (L. Smith, personal communication).

It is claimed that the breeding method mimics the analysis cycle that is used to generate operational initial conditions. As a result, it is argued that analysis errors will tend to rotate into the direction of the breeding vector. As discussed in section 3.3 below, the singular vectors form the basis for the calculation of initial perturbations for the ECMWF ensemble prediction system. How do the growth and spectrum of the breeding vectors compare with the singular vectors?

In order to discuss this question, I would like to show some results from a set of

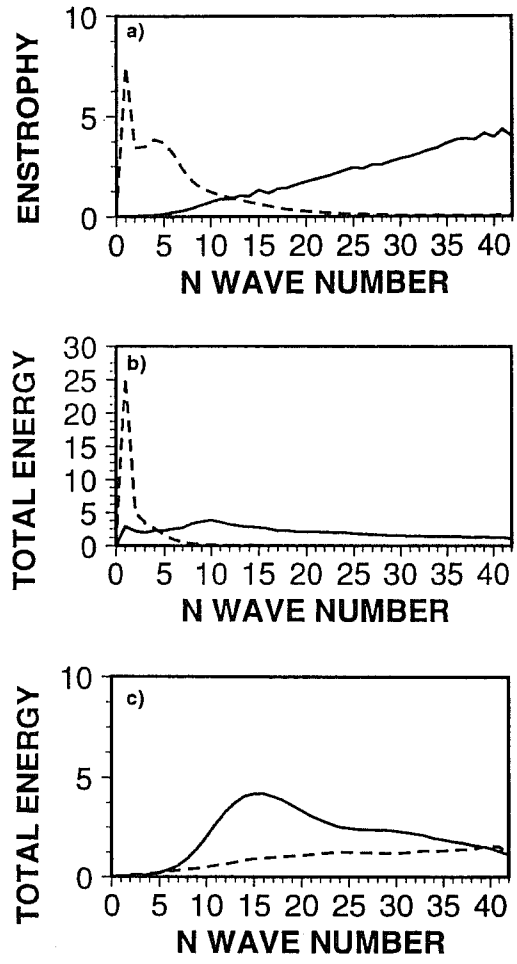

Figure 2.3: (a) Average enstrophy (s^{-2}) spectrum of the first 16 enstrophy-SVs at initial (dash, $\times 40\ 10^{16}$) and final (solid, $\times 10^{16}$) time, (b) average energy (per unit mass) spectrum ($m^2\ s^{-2}$) of the first 16 energy-SVs at initial (dash, $\times 40$) and final (solid, $\times 40$) time, and (c) average energy spectrum of the first 16 energy-SVs at initial (dashed, $\times 40$) and final (solid) time, for 6 April 1994. From Molteni *et al* (1996).

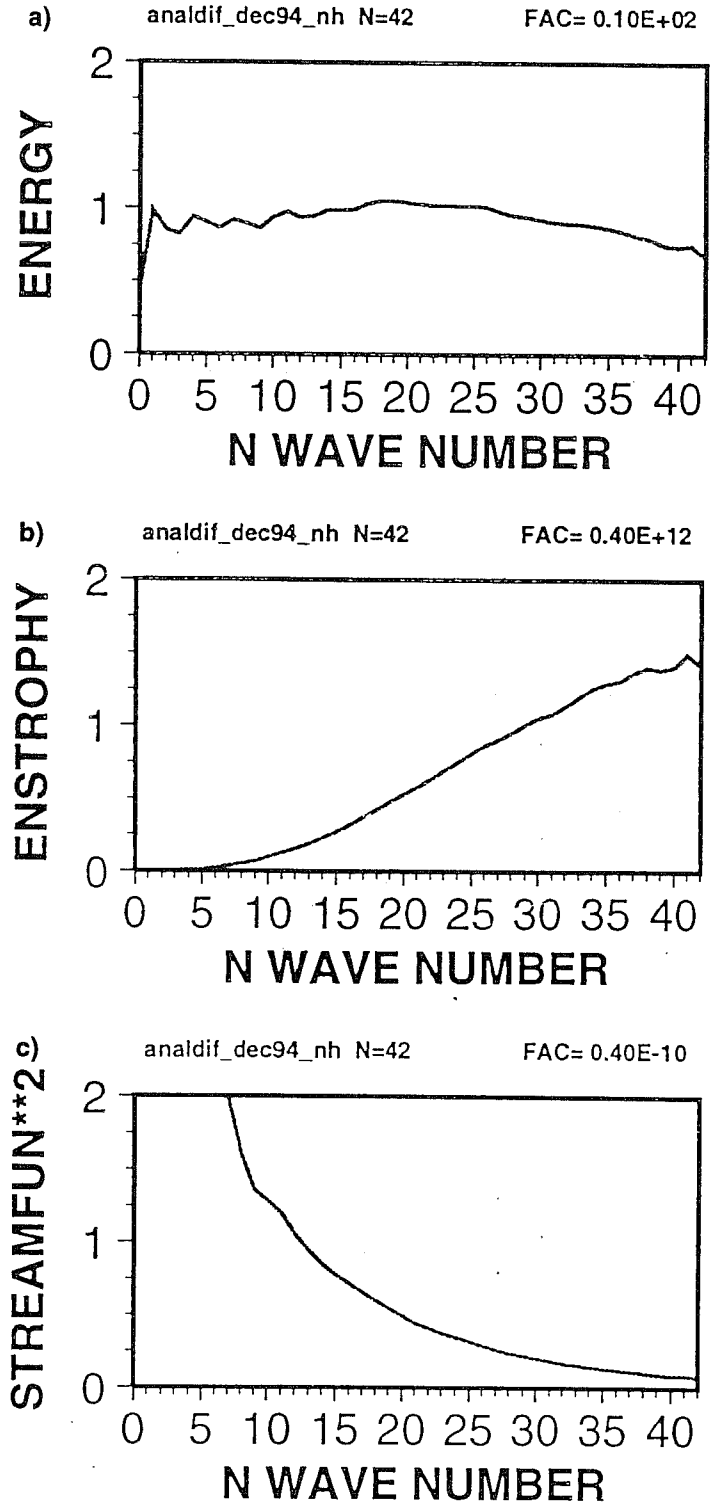

Figure 2.4: The mean 2D total wavenumber spectrum of analysis difference fields in terms of a) energy, b) enstrophy, c) streamfunction variance. This mean has been calculated over 42 analysis difference fields, based on experimental operational analysis code and the operational suites at ECMWF. The experimental suites involve both different model formulations and different analysis technique (R. Gelaro, personal communication).

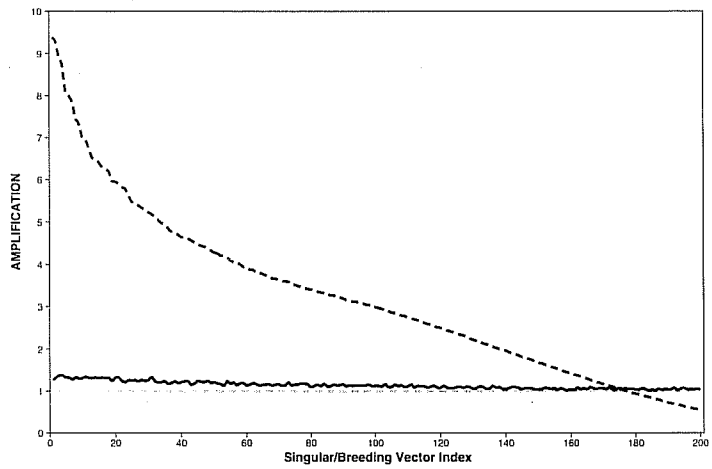

Figure 2.5: The growth of orthogonal perturbations produced by the breeding method (solid line) and the singular vector method (dashed line), over a typical 12 hour period, based on the T21L3 quasi-geostrophic model of Marshall and Molteni (1993) (J. Barkmeijer, personal communication).

integrations of a 3-level quasi-geostrophic model (as formulated by Marshall and Molteni, 1993). In these integrations, the spectrum of breeding vectors has been compared with the spectrum of singular vectors over a 12 hour cycle time (for the breeding method) and a 12 hour optimisation time (for the singular vectors). These calculations have been performed by J. Barkmeijer (personal communication).

Fig 2.5 shows a typical spectrum for the singular vectors and the breeding vectors. The spectrum of the breeding vectors is very flat. The fastest growing perturbation grows by a factor of 1.4, the 200th perturbation grows by a factor of 1.1. In fact there are typically between about 250 and 300 growing directions as determined by the breeding method. By contrast the dominant singular values are much faster growing, and decay more rapidly with singular vector number. The fastest growing singular vector grows by a factor of 9.3, the 200th perturbation is actually decaying. In fact it can be shown that because of the flat spectrum, even small amounts of nonlinearity prevent the breeding vector from converging to a Lyapunov vector.

It can be asked whether the dominant singular vectors and breeding vectors correlate with one another. In general they do not. At initial time the singular vectors are dominated by sub-synoptic scales, whilst the breeding vectors are dominated by synoptic scales (for stationary basic states they would be given by the synoptic-scale eigenmodes). As such their spatial correlation is close to zero. At optimisation time, the singular vectors evolve towards synoptic scales and the correlation with the dominant breeding vectors increases, though only to values of about 0.2 (in the T21QG model).

Using these results, and those from the last section, I believe that it is possible to make the following conclusions about the relationship between the breeding vectors and the PDF of analysis error. Firstly, since the spectrum of breeding vectors is extremely flat, there is no particular reason why the analysis error should project more onto the leading breeding vectors. Of course, if one had enough breeding vectors (and if they were suitably orthogonalised) then any perturbation, including the analysis error, should project into the space spanned by these vectors. However, it appears from the results above that the number of such vectors would have to be a significant fraction of the phase space dimension.

In fact, in my opinion, even if the spectrum of breeding vectors was in fact much

steeper, it is questionable whether the analysis error would ever rotate into the direction of a leading breeding vector. The reason for this is to do with the role of observations in the analysis cycle. As discussed *eg* by Hollingsworth (1987) and Daley (1991), operational analyses blend observations with a first-guess field in a scale-dependent manner. On large scales, the observations carry more weight than the first guess field, whilst on small scales the first guess carries more weight than the observations. Therefore, in my opinion, to represent the role of observations, one would require, within each breeding cycle, the breeding vector to undergo a phase-space rotation (and not just a renormalisation as is actually done). This phase-space rotation would continually 'frustrate' the breeding vector's attempt to rotate towards some dominant Lyapunov direction.

The NMC assumption that analysis errors rotate into a selection of preferred directions can be compared with the ECWMF philosophy in which (*cf* section 2g) it is assumed that there are, in fact, no preferred phase-space directions for the analysis error (*ie* with respect to a suitable inner product, the PDF of analysis error is relatively isotropic). This assumption has been verified for local European forecasts by Barkmeijer *et al* (1993).

There is one other important difference between the breeding and singular vector methodology. The singular vectors are computed over the period in the immediate future of the initial analysis, whilst the breeding method refers to the period leading up to the initial analysis. This is why singular vector perturbations define, amongst all the *a priori* equally-likely initial directions, those which give rise to the largest possible forecast error.

Nevertheless, perturbations using both breeding vectors and singular vectors have proven useful for medium-range ensemble prediction. It is possible that differences between the two techniques becomes less important as one evolves towards the 'strongly nonlinear' PDF regime (see Fig 2.1).

3 EXAMPLES OF SINGULAR VECTORS

3.1 A baroclinic singular vector

Fig 3.1 shows the dominant singular vector calculated using the ECMWF primitive equation model (Simmons *et al*, 1989; Courtier *et al*, 1991), for a 3-day trajectory portion made from initial conditions on 9 January 1993, at three levels in the atmosphere (200 hPa, 700 hPa and 850 hPa) at initial and optimisation time. The figure illustrates some features which bear qualitative resemblance to an idealised baroclinic eigenmode (Charney, 1947; Eady, 1949): the disturbance clearly amplifies as it propagates through the region of maximum baroclinity (where north-south temperature gradients are strongest), and the disturbance shows evidence of westward tilting phase with height, consistent with a northward flux of heat.

On the other hand, the figure also clearly illustrates the non-modal nature of the disturbance. At initial time the disturbance is localised near the north Atlantic jet entrance region; at optimisation time the disturbance has propagated downstream to Europe. At initial time, maximum disturbance amplitude is located in the lower troposphere, whilst at optimisation time maximum amplitude is located in the upper troposphere at the level of maximum winds (*cf* Farrell, 1989). Finally, the horizontal scale of the initial disturbance is noticeably smaller at initial time than at optimisation time.

As discussed in section 2, singular-vector structure can be related to the Orr (1907) process for transient growth (in asymptotically stable flows). As discussed in Lindzen (1988), the Orr mechanism essentially operates in shear flow from a critical layer. The vertical structure of the singular vectors underpins this relationship. For example, under

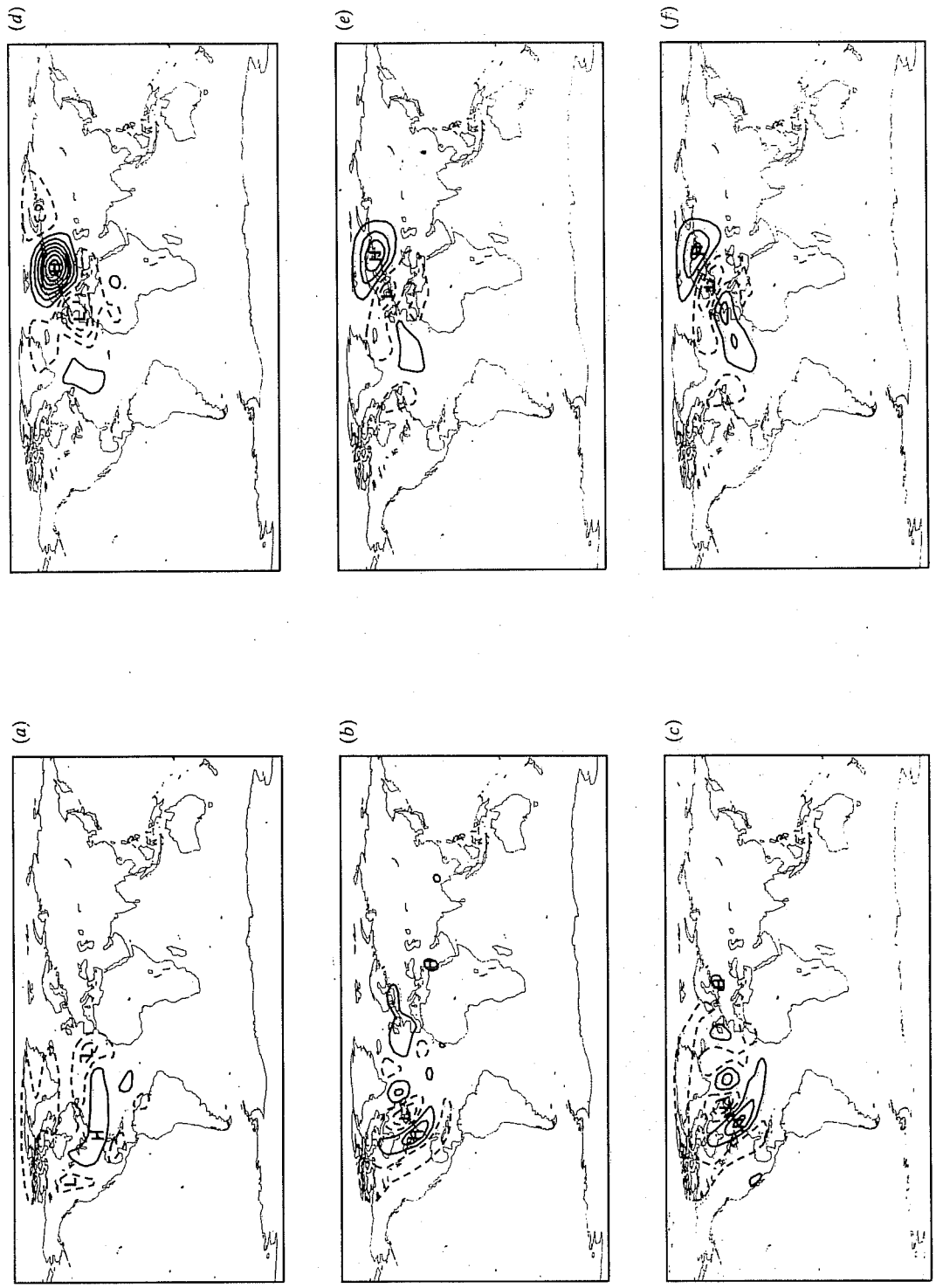

Figure 3.1: Streamfunction of the dominant atmospheric singular vector calculated using a primitive equation numerical weather prediction model for a 3-day trajectory portion made from initial conditions of 9 January 1993 at three levels: 200 hPa a) d), 700 hPa b) e), 850 hPa c) f). a)-c) - initial time. d)-f) - optimisation time. Contour interval at optimisation time is 20 times larger than at initial time. From Buizza and Palmer (1995)

certain assumptions (steady zonally symmetric basic state flow which is slowly varying in the vertical) the wave-action $E/(\omega - ku_0)$ of a linear disturbance with energy E, zonal wavenumber k and frequency ω will be conserved as it propagates vertically on the background flow u_0. Optimal energy growth will tend to be associated with propagation from a region of small intrinsic frequency (near the baroclinic steering level, to a region of large intrinsic frequency (such as might occur near the jet level).

The horizontal-scale evolution of the singular vector is explored further in Fig 3.2 which shows the energy distribution of the singular vector at initial and final time, as a function of total wavenumber. Fig 3.2a shows the spectral distribution of the disturbance shown in Fig 3.1 peaking near the truncation limit at initial time (dashed line) and at about wavenumber 10 at optimisation time. This upscale energy transfer can occur because the basic state (unlike those in many idealised calculations) is itself an unrestricted solution to the equations of motion, and, in particular contains scales comparable with those in the disturbance field. This allows triad interactions between the disturbance field and the basic state.

Fig 3.2b,c shows the spectral distribution of two further singular vector calculations made using the same trajectory. In these calculations, the spectral projection operator (2.17) has been applied both at initial and optimisation time. For both calculations, the operator at optimisation time maximises energy between wavenumbers 0 and 10. The initial perturbation is constrained to wavenumbers 0-10 in Fig 3.2b and to wavenumbers 11-20 in Fig 3.2c.

The results are quite dramatic. Constraining the perturbation to have the same energy distribution in wavenumber space at initial and final time (which an eigenmode solution, if it exists, must have), severely restricts perturbation growth. On the other hand, constraining the perturbation at initial and final time to have energy in non-overlapping wavenumber intervals hardly restricts energy growth at all (see Hartmann *et al*, 1995, for more details).

These calculations illustrate, in a linear context, the 'butterfly effect' in its original sense (Lorenz, 1963b), *ie* that small-scale initial disturbances can ultimately have an overwhelming influence on large-scale disturbances. This is in addition to the commonly perceived meaning of the butterfly effect that small-amplitude initial disturbances will ultimately have an overwhelming effect on large-amplitude disturbances. (In fact, Lorenz refers to the influence on the weather of a flap of a sea-gull's rather than a butterfly's wings. In view of the location of the initial singular vectors over the west Atlantic ocean, rather than, say, over Amazonia, this original metaphor is in this case fortuitously appropriate!). The upscale cascade associated with the butterfly effect has been modelled in a turbulent rotating fluid context by Lilly, 1983 and Metais *et al*, 1994 (see also section 3.2).

The accumulation of initial energy towards the truncation limit suggests that a significantly more accurate estimation of singular vector growth should be obtainable using a higher resolution model. In fact studies using a T42 resolution tangent model confirm this (Hartmann *et al*, 1995; Buizza *et al*, 1996). With this resolution, a significant fraction of perturbation energy is located at subsynoptic scales at initial time, cascading to synoptic scales at optimisation time (see also section 3.2). One practical consequence of this result is that the predictability of synoptic scale weather may be determined more by uncertainties in the initial state on scales much smaller than the disturbance itself, and less by uncertainties on the scale of the disturbance. In particular, the notion that the predictability of synoptic scale weather is determined by the e-folding time of a characteristic eigenmode is incorrect (confirming earlier results of Farrell, 1990).

As mentioned, although the structures of these baroclinic singular vectors are not

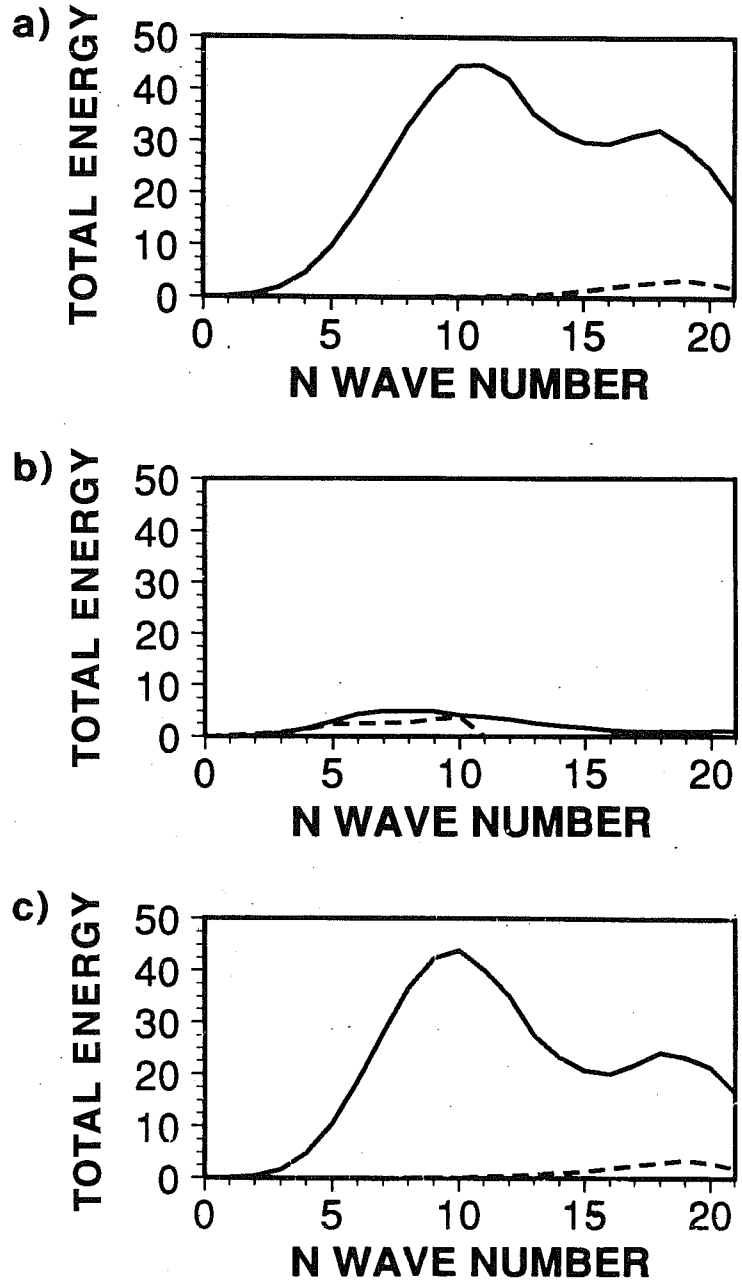

Figure 3.2: Energy distribution of 3-day singular vector from 9 January 1993 as a function of (total) wavenumber. Dashed - at initial time (x20). Solid - at optimisation time. a) For singular vector shown in Fig 3.1 b) For singular vector with energy optimised for wavenumbers 0-10, and constrained to wavenumbers 0-10 at initial time. c) For singular vector with energy optimised for wavenumbers 0-10, and constrained to wavenumbers 11-20 at final time. From Palmer *et al* (1994).

modal, their geographical locations are more prevalent in regions of strong baroclinity. Fig 3.3a for example, shows the 'Eady index'

$$\sigma_E = 0.31 \frac{f}{N} \frac{du}{dz} \tag{3.1}$$

based on the a winter mean static stability and wind shear (from ECMWF data; for details see Buizza and Palmer, 1995). (Of course the functional relationship between the wind shear, Coriolis parameter and static stability in 3.1 are not particular to the Eady model). Fig 3.3b shows the location of the dominant singular vectors at initial time (based on their vorticity maxima) from daily calculations over a whole winter. It can be seen that the singular vectors tend to be positioned in regions of strong Eady index, over the east Asian/west Pacific region, the northeast American/west Atlantic region, and the northern subtropical African region. The tropics and southern hemisphere extratropics also appear in these northern winter statistics, though to a lesser extent.

3.2 Pseudo-Inverse Analysis

In terms of the singular vectors, we can decompose the forward tangent propagator $\mathbf{L}$ as,

$$\tilde{\mathbf{L}} = \mathbf{U}\mathbf{\Sigma}\mathbf{V}^* \tag{3.2}$$

where $\mathbf{V}$ contains the initial singular vectors, $\mathbf{U}$ the final singular vectors, and $\mathbf{\Sigma}$ is a diagonal matrix with elements σ_i. Within the subspace spanned by the dominant singular vectors, we can define the inverse

$$\tilde{\mathbf{L}}^{-1} = \mathbf{V}\mathbf{\Sigma}^{-1}\mathbf{U}^* \tag{3.3}$$

In terms of the full phase space, $\tilde{\mathbf{L}}^{-1}$ is related to the Moore-Penrose pseudo-inverse (for more details, see Buizza *et al*, 1996).

By operating on a given forecast error field with the pseudo-inverse operator, an estimate of the unstable component of initial error is obtained. Some examples of this pseudo-inverse field are shown in Buizza *et al* (1996) based on a 30 singular vector truncation, and a 36-hour forecast error. By adding this estimate to the initial analysis, a much superior forecast can be obtained, not only at 36 hours, but throughout the entire medium-range. It should be noted that the pseudo-inverse component of initial error may be small compared with the total error. Indeed, associated with the non-invertibility of the full operator $\mathbf{L}$, the forecast error will be insensitive to estimates of initial error in strongly decaying directions.

This technique is closely related (but not identical) to the sensitivity analysis technique (see section 3.5) in which the forecast error is integrated (backwards) using the adjoint model itself (see Rabier *et al*, 1996; Buizza *et al*, 1996).

3.3 Comparison of tropical and extratropical singular vector growth: a paradigm for tropical predictability.

It is clear from numerous studies that the large-scale tropical circulations are much more strongly coupled to the underlying SST than are large-scale extratropical circulations. As such, the prospects for extended-range prediction in the tropics are greater than for the extratropics. Charney and Shukla (1981) were one of the first to rationalise this disparity in behaviour between the tropics and extratropics. These authors argued that, from a

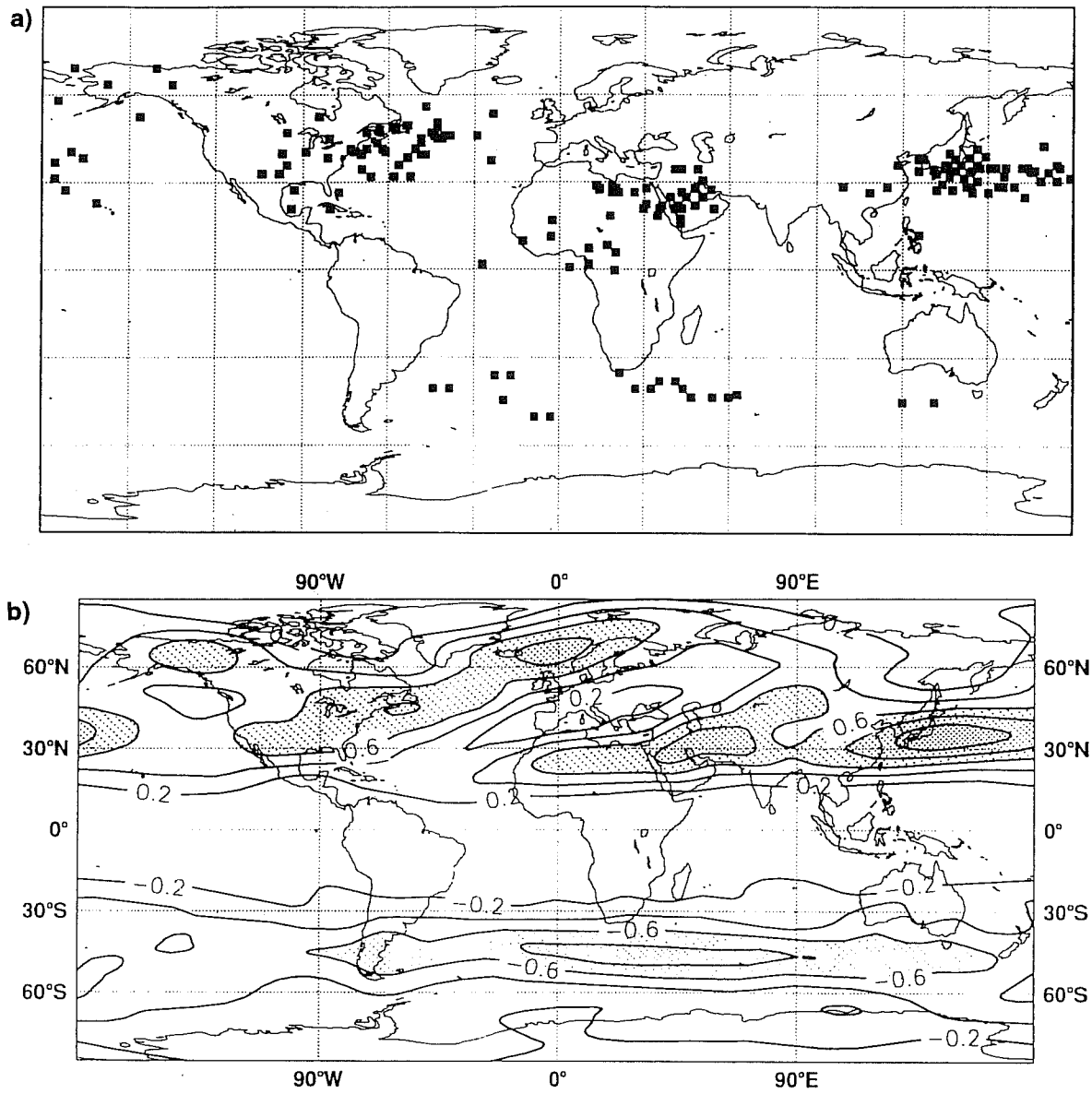

Figure 3.3: a) Distribution of dominant singular vectors for a winter season. The position of a singular vector is denoted by a black dot at the vorticity maximum at initial time. b) Eady index (3.1) based on seasonal mean flow. From Buizza and Palmer (1995).

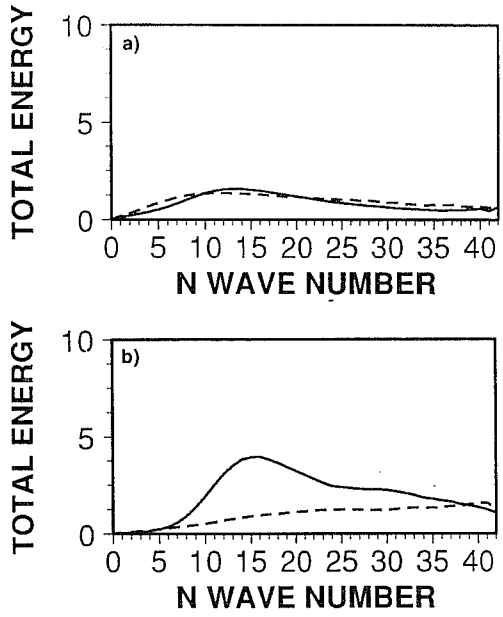

Figure 3.4: Total wavenumber spectrum of mean energy the dominant 18 48-hour singular vectors a) optimised over the tropics, b) optimised over the northern hemisphere extratropics. The initial spectrum (x40) is given by the dased lines, the final spectrum is given by the solid lines. The tangent propagator for these calculations had a T42 resolution.

dynamical point of view, the principal relevant difference between the large-scale tropical and extratropical flows lay in their instability properties. The absence of generic large-scale exponentially growing eigenmodes in the tropics makes more reproducible the effects of slowly-varying lower boundary conditions associated, for example, with SST anomalies.

Whilst these considerations are clearly important and relevant, they cannot be considered complete. For example, the tropical flow is convectively unstable, and these in turn contribute to the growth of synoptic-scale disturbances, *eg* associated with tropical cyclones. However, it is known that inevitable errors in the initial conditions for atmospheric seasonal integrations associated with tropical synoptic and subsynoptic flow, do not infect the planetary scale circulations in the same ubiquitous way that is found in the extratropics.

It is manifestly impossible to describe this difference in upscale energy cascade using modal instability theory. On the other hand, as we have seen in the last section, singular vector analysis is able to describe, within a completely linear framework, the inverse cascade process associated with extratropical baroclinic growth.

Let us compare the spectrum of singular vectors calculated for extratropical and tropical growth respectively. Fig 3.4 shows the spectrum of the first 18 singular vectors for a particular (but typical) 36-hour period based on the T42 tangent model. Fig 3.4a shows growth optimised for the tropics; Fig 3.4b shows growth optimised for the extratropics. The solid line shows the energy of the singular vectors at optimisation time, the dashed lines show the energy at initial time (multiplied by a factor of 40 to make them more visible on the diagram).

The singular values for the extratropics are larger than those for the tropics. In addition, the spectrum of tropical singular vectors is considerably more modal than the extratropical spectrum. The spectrum peaks in the large synoptic scale, and therefore indicates that error growth at these scales will not be dominated by error growth from smaller scales.

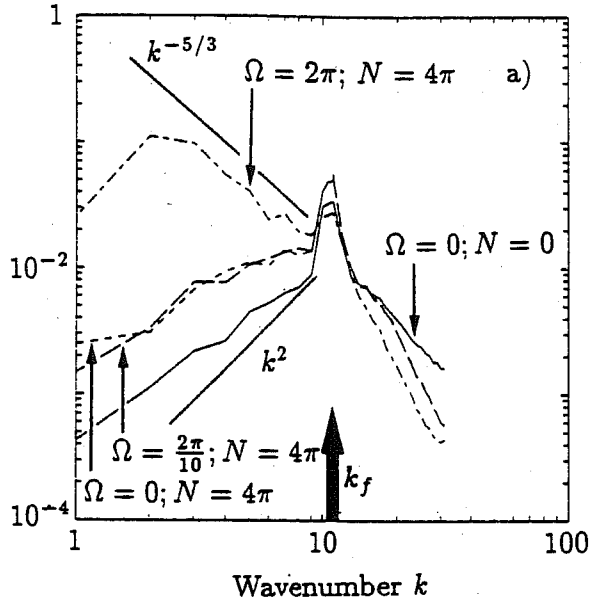

Figure 3.5: Wavenumber spectrum of kinetic energy of a laboratory turbulent fluid forced at an intermediate wavenumber, for various rotation and stratification values. From Metais *et al* (1994).

These results appear consistent with studies of inverse energy cascades in fully-developed turbulence models, in which the Coriolis parameter is varied. Fig 3.5 (from Metais *et al*, 1994) shows the spectrum of kinetic energy in a stratified turbulent fluid forced at an intermediate wavenumber (shown by the heavy arrow), for various rotation rates and stratifications. Results show that in a strongly rotating regime, the energy spectrum is an increasing function with increasing scale. However, in the nonrotating case, the energy decreases with decreasing wavenumber. The influence of rotation appears to be associated with the dimensionality of the associated turbulence fields, and this dimensionality determines the upscale cascade.

Hence, singular vector analysis is apparently able to distinguish between the different cascade processes in low and high rotation rate regimes, and this, as much as the intrinsic modal instability properties of the flow, may be important in distinguishing between the different predictability regimes in the tropics and extratropics. This may be important in understanding the predictability of ENSO. Sarachik (1990), for example, discussing an intermediate coupled ocean-atmosphere model of the tropical Pacific (see section 3.6 for more details) notes that '..whenever the [model's] mean state is unstable, the resulting cycle is perfectly regular: instability (in this model) is therefore related to perfect predictability'. Sarachik then notes that '..This paradigm of ENSO predictability is radically different from our classical concepts of mid-latitude predictability'. However, Sarachik does not explain why there should be two paradigms: one for the tropics, the other for the extratropics. A possible explanation could be given in terms of the modality of the associated singular vectors. In contrast with tropical singular vectors, the extratropical singular vectors are profoundly non-modal and perturbation growth is therefore susceptible to the 'butterfly effect' (*cf* above). As discussed above, this non-modality and associated upscale cascade can cause extratropical weather forecasts to fail before the timescale set by any characteristic e-folding rate.

3.4 Singular Vectors for Ensemble Forecasting

Singular vectors are used as the basis of initial perturbations for medium-range ensemble forecasting. The basic rationale for this is that we cannot sample explicitly, analysis uncertainties in all the phase space directions, the dimension of a numerical weather prediction model (at least $O(10^6)$) is too large. Hence we sample explicitly directions in which analysis error is likely to occur and can lead to significant departures from the unperturbed forecast. In the linear regime these are given by the dominant singular vector directions. Hartmann *et al* (1995) have shown that up to about day 7, perturbations using singular vectors have significantly larger spread than unstable synoptic-scale perturbations. This would suggest that the 'weakly nonlinear' timescale (*cf* section 2.1) lasts until about day 7.

Other directions (for example associated with decaying perturbations) can in principle be taken implicitly into account in an ensemble forecast by giving the unperturbed forecast a higher than average *a priori* weight compared with other members of the ensemble.

Fig 3.6 shows two examples of ensemble forecasts made from initial conditions one week apart. The thin lines show the spread of the members of the ensemble forecast relative to the unperturbed control forecast (using a correlation measure of spread). The thick line shows the skill of the control forecast (using a correlation measure of skill). The examples illustrate the desirable occurrence of low spread indicating high skill, and high spread indicating relatively poor skill.

Obviously one cannot make any definitive conclusions based on just two results. The interested reader is directed to a more complete description and validation of the ECMWF ensemble prediction system in Molteni *et al* (1996).

3.5 Weather Regimes, Singular Vectors and Sensitivity Patterns

The concept of weather regimes is a long standing one (*cf* Grosswetterlagen; Hess and Brezowsky, 1977), and is based on the notion that the large-scale flow may evolve around various recurrent configurations. This notion was made more precise in modelling studies (Reinhold and Pierrehumbert, 1982) who related the onset, maintenance and decay of regimes to interactions of the large-scale flow with synoptic-scale variability. The existence of such weather regimes in the real atmosphere has been inferred through observational studies (*eg* Hansen and Sutera, 1986, 1995; Mo and Ghil, 1988, Molteni *et al* , 1990, Cheng and Wallace, 1993, Kimoto and Ghil, 1993), though the existence of unambiguous multimodality is still a matter of debate (Wallace *et al*, 1991). In many observational studies, (*eg* Yang and Reinhold, 1991; Dole and Gordon, 1983 and Toth 1992), it is suggested that baroclinic instability sets the timescale for the transition process betweeen regimes. This timescale is much shorter than a typical residence timescale (on the order of weeks). This two-timescale behaviour is consistent with the regime structure in the 3-component Lorenz model (see Fig 4.3 below).

Fig 3.7 shows two of the large-anomaly cluster centroids found by Mo and Ghil (1988) (3.7a and 3.7b) and by Molteni *et al* (1990) (3.7c and 3.7d). Despite different clustering algorithms, Figs 3.7a and c correspond to one another quite well (as do Fig 3.7b and d). The regime centroids have significant projection onto opposite phases of the Pacific North/American (PNA) pattern (Wallace and Gutzler, 1981), though also have structure over the Atlantic and EurAsia (*cf* section 6 on climate change). By convention, the PNA index of the fields in Fig 3.7a and c is positive, the PNA index of the fields in Fig 3.7b and d is negative. For future reference, Molteni *et al* (1990) refer to Fig 3.7c as cluster 2,

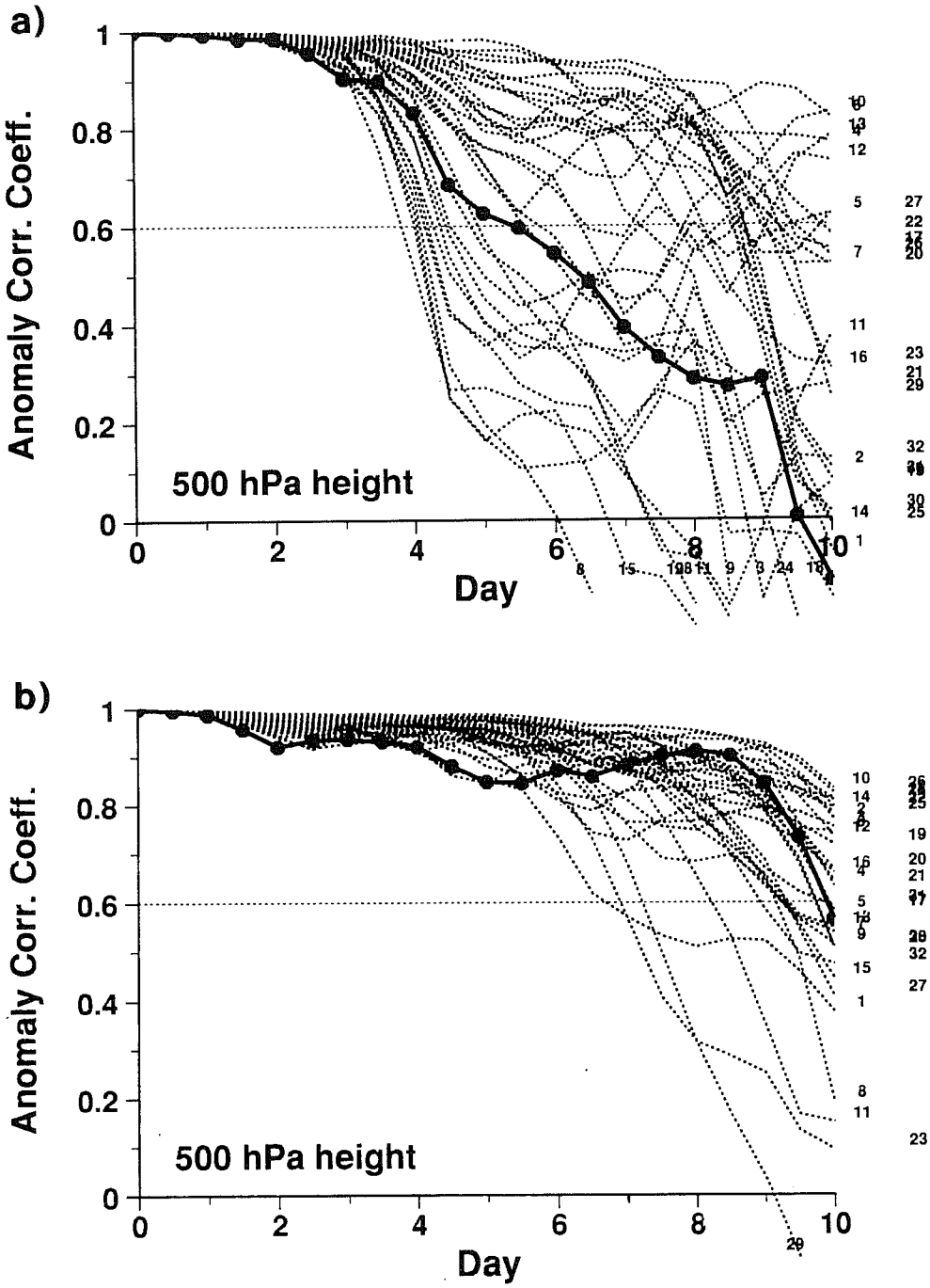

Figure 3.6: Ten-day ensemble forecast dispersion as measured by anomaly correlation between 500 hPa geopotential height of control and perturbed forecasts, over Europe (light lines). Skill of 10-day control forecast (heavy line), a) forecasts from 30 October 1993, b) forecasts from 13 November 1993. From Palmer *et al* (1994).

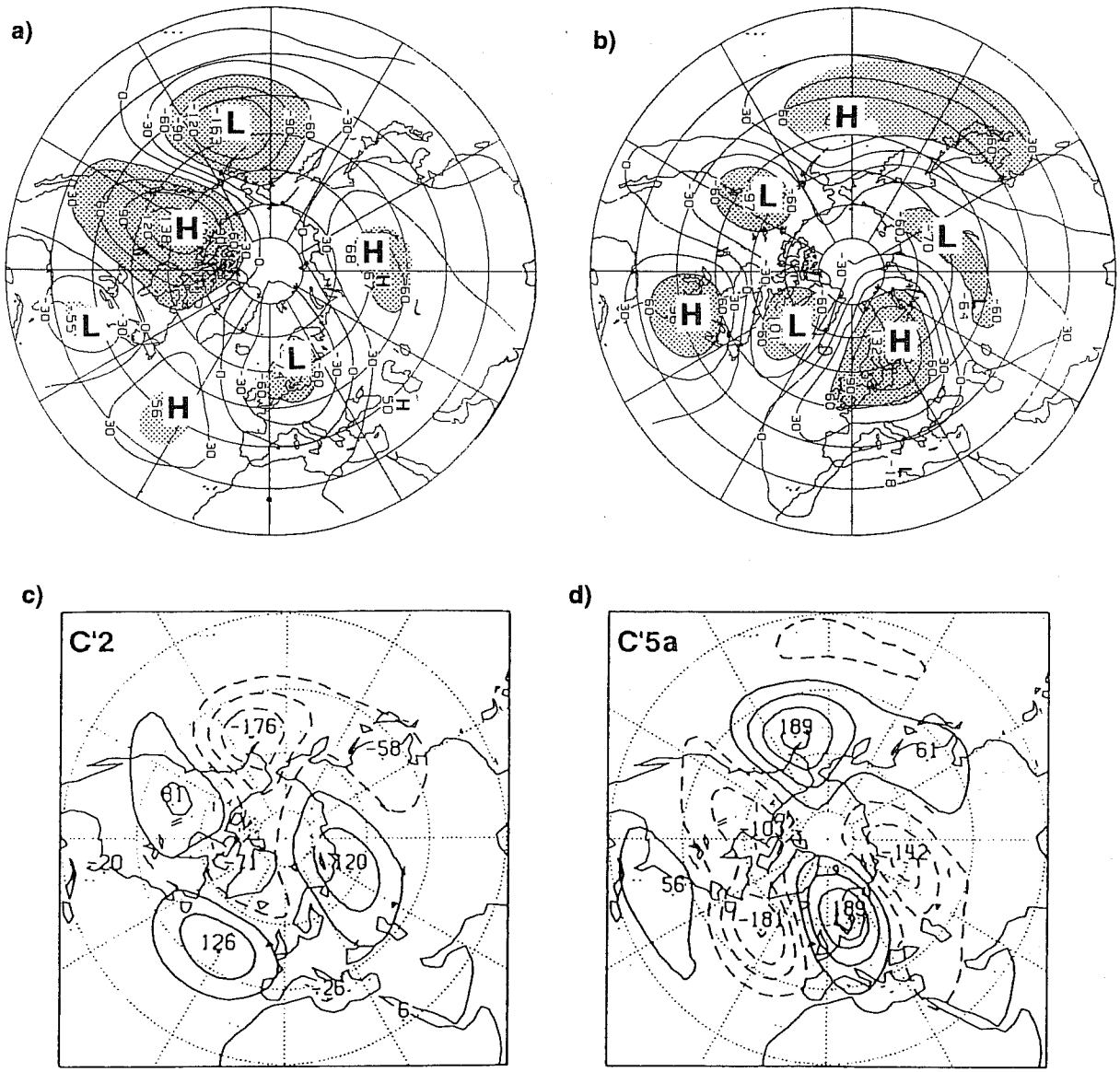

Figure 3.7: Anomalies corresponding to the centroids of clusters 1 and 2 (a and b) found by Mo and Ghil (1988), and of clusters 2 and 5 (c and d) found by Molteni *et al* (1990). In a) and b), shading indicates statistical significance at the 95% confidence level.

and Fig 3.7d as cluster 5.

Regimes can also be found in atmospheric model integrations. Fig 3.8a shows the PDF from a 100 consecutive winter sample of a 1200 perpetual-winter integration of a 3-level T21 quasi- geostrophic model (Marshall and Molteni, 1993; Corti, 1994; Palmer *et al*, 1994). The PDF is estimated in a phase-space plane spanned by two of the dominant empirical orthogonal functions of the model (shown in Fig 3.8b). During this chosen 'century', the PDF is bimodal along an axis that corresponds to fluctuations in the North Atlantic Oscillation.

As shown in Palmer (1988), low-frequency intraseasonal variability is stronger over the PNA area during periods when the atmosphere resides in negative PNA states, than positive. Consistent with this, medium-range forecasts are more skilful during positive PNA periods (Molteni and Tibaldi, 1990). On longer timescales, it has been found from both modelling and observational studies (Von Storch, 1988; Chen and Van Den Dool, 1996) that there is less low frequency intraseasonal variability over the PNA region during warm-phase ENSO winters than cold-phase ENSO winters.

Evidence of variations in the instability characteristics of positive and negative PNA states was discussed in Palmer (1988), who found that the growth of linear perturbations in a barotropic model depended strongly on the sign of the PNA index of the basic-state flow. However, it was noted that the difference in these growth rates could not be explained in terms of differences in the eigenmode growth associated with the basic states. Molteni and Palmer (1993) compared the growth rates of the fastest-growing eigenmodes and the optimal singular vectors for the cluster 2 and cluster 5 flow in the barotropic model. For the most unstable eigenmode (which is stationary in both cases) there is little difference in growth rates for the two basic states. On the other hand, the dominant singular values are quite different. In particular, for 8-day optimisation, the dominant singular value for the cluster 2 flow is almost a factor of 2 smaller than that of the cluster 5 flow. The streamfunction of the final dominant singular vector for an 8-day optimisation is shown in Fig 3.9 for the cluster 2 and cluster 5 basic states.

There are two important approximations that have been made in these calculations. The first is the use of a barotropic model. The second relates to the fact that we have chosen stationary basic states which are not themselves solutions of the equations of motion. With regard to the second approximation, the error involved in using a stationary basic state should at least be smallest for those states corresponding to observed cluster centroids, since, by construction, these are, in some ensemble sense, closest to stationary.

The approximation involved in using the barotropic model is actually not as bad as might be imagined at first sight. According to results in Molteni and Palmer (1993), 8-day singular vectors of a realistic time-varying baroclinic basic state are (at final time) more accurately represented by a time-averaged barotropic basic state than by a time-averaged baroclinic basic state. The reason for this is that the instability of a time-averaged baroclinic flow will tend to overly dominated by the baroclinic instabilities which relate directly to the meridional thermal contrasts. Moreover, since the Rossby-wave structures of such time-averaged flows are under-represented, the upscale cascade process discussed in section 3.1 is weak. As a result, singular vectors from time-averaged baroclinic flows tend, at final time, to be dominated by smaller scales than would occur with a time-varying flow. By contrast singular vectors from time-averaged barotropic basic states (which also evolve through upscale energy evolution) are dominated at final time by larger, more realistic scales.

It is of interest to ask, however, how one might go about calculating regime instabilities without using such approximations. Let us represent the regime centroid by the a given

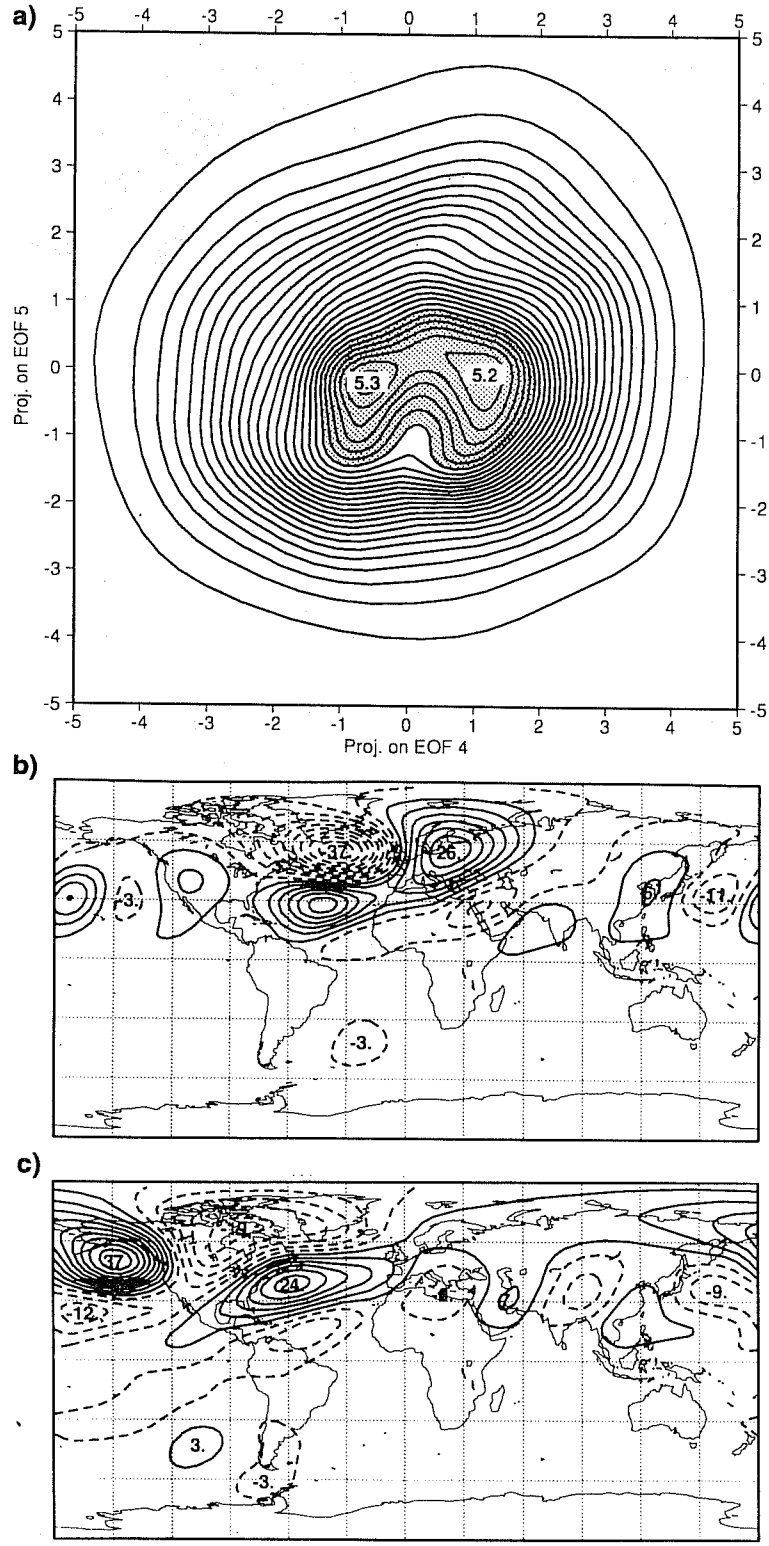

Figure 3.8: a) 2-D cut of the PDF from 100 consecutive winters of a multi-decadal integration in the T21L3 quasi-geostrophic model of Marshall and Molteni (1993). b), c) The model empirical orthogonal functions, used to define the axes in a). From Palmer *et al* (1994).

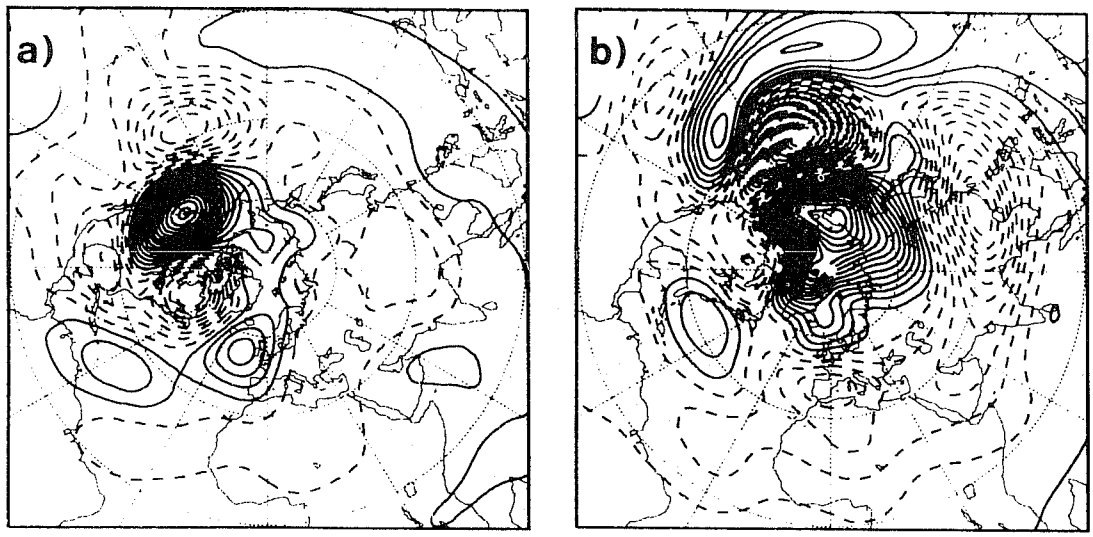

Figure 3.9: 500hPa stream function of dominant barotropic day-8 singular vector at day 8 for (a) cluster 2 and (b) cluster 5 of Molteni *et al* (1990). From Molteni and Palmer (1993).

normalised large- scale pattern $E(x, y, z)$. One possibility is to compute the pseudo-inverse of $E(x, y, z)$ using the dominant singular vectors, for a variety of finite-time trajectories. A less computationally demanding, but largely equivalent calculation can be achieved with a single integration of the adjoint model. Suppose we want to find a perturbation, with unit norm at initial time, and maximum projection onto the given pattern E at final time. In symbols, we want a perturbation e at $t = t_0$ which at $t = t_0 + \Delta t = t_1$ maximises $< Le, E > / < e, e >$. This perturbation will be given at $t = t_0$ by $e = L^* E$. We can refer to e as the sensitivity pattern (*cf* Marchuk, 1974; Cacuci, 1981; Rabier *et al*, 1995) for E, and the growth $||Le||/||e||$ as the instability index of E. Such work is currently in progress using a three-level quasi-geostrophic model whose climatology, as shown above, has realistic regime structures (Susanna Corti, personal communication). These calculations could be of particular interest in studying the sensitivity of observed climate change patterns (see section 6).

3.6 Singular vectors from a coupled tropical ocean-atmosphere model

ENSO appears to be predictable up to a year or so in advance using relatively simple coupled models of the atmosphere and ocean (Zebiak and Cane, 1987). According to Münnich *et al* (1991), long-term variability of ENSO is intrinsically chaotic (independent of the chaotic nature of weather itself). The skill of ENSO forecasts made with coupled ocean-atmosphere models is seasonally dependent (Cane *et al*, 1986; Webster, 1995). Typically, seasonal forecasts beginning in spring tend to be less skilful than forecasts beginning, for example, in autumn. This is sometimes referred to as the 'spring barrier' effect.

Blumenthal (1991) has analysed the behaviour of the eigenfunctions of a linear Markov model approximation to a nonlinear coupled ocean-atmosphere model. He finds that in summer, the eigenfunction best describing ENSO has larger eigenvalues than at other times of year. In spring this ENSO eigenfunction is least orthogonal to other modes, *ie* is associated with large projectibility (see section 2). Both types of error growth (modal and non-modal) are implicit in singular vector analysis which has been performed on this Markov model by Xue *et al* (1994).

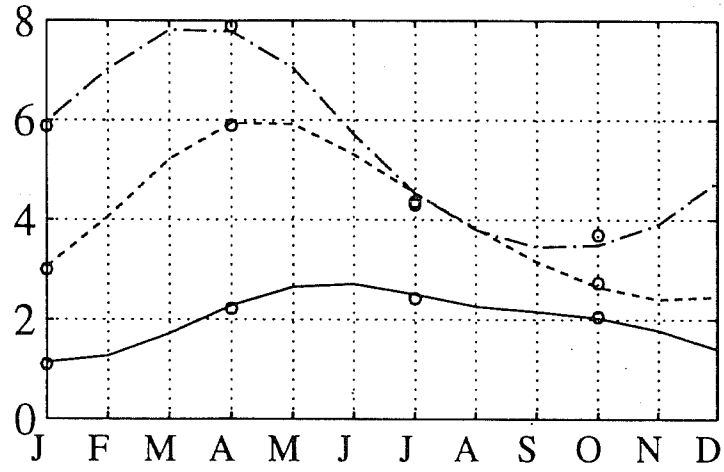

Figure 3.10: Dominant singular values for 3-month (solid), 6-month (dashed) and 9-month (dashdot) from the Battisti (1988) intermediate coupled ocean atmosphere model. The basic state trajectory is a climatological annual cycle. From Chen *et al* (1996).

We show some results of a singular vector analysis applied to the coupled ocean-atmosphere model of Battisti (1988). Preliminary results were described by Palmer *et al* (1994), more extensive results are given in Chen *et al* (1996). A similar study has been performed independently by Moore and Kleeman (1996). The ocean component of the model used here is a single vertical mode tropical Pacific basin anomaly model, governed by linear shallow water wave dynamics. The nonlinear thermodynamics are only active in a surface mixed layer. The atmospheric component is a thermally -forced steady linear model with single vertical mode (Gill, 1980). Air-sea interactions are nonlinear: given by surface wind stress, heat flux, and sea surface temperature, SST. The number of independent degrees of freedom in the coupled model is reduced to 420 by considering only the equatorial oceanic Kelvin mode, and first 3 symmetric Rossby modes. With such a reduction, singular vectors can be computed using conventional matrix algorithms. For these calculations, the inner product is based on the spatial variance of the SST anomaly.

The first results have been made using a climatological basic state flow. Perturbation growth is strongly dependent on the annual cycle in the Pacific, and on the duration of the integration. Fig 3.10 shows the dominant singular values for 3-, 6-, and 9-month optimisation times. (The optimisation time is greater *eg* than in section 3.1 because of the longer predictability time associated with ENSO.) The maximum singular vector for the 6-month integration ranges from 6 for the April start, to less than 3 for the October start. The results point to a period of greater sensitivity during the boreal spring and summer.

In contrast with the sensitivity of the singular values, the pattern of both initial and final state singular vectors are relatively insensitive to the month in which the initial perturbation is applied, and to the duration over which the error is allowed to grow. For example, Fig 3.11 shows the SST of the singular vectors (at initial and optimisation time) for 6-month optimisation based on starting conditions for January, April, July and October. The initial pattern consists of an east-west dipole spanning the entire tropical Pacific basin, superimposed on a north-south dipole in the eastern tropical Pacific. The pattern at optimisation time resembles the ENSO mode.

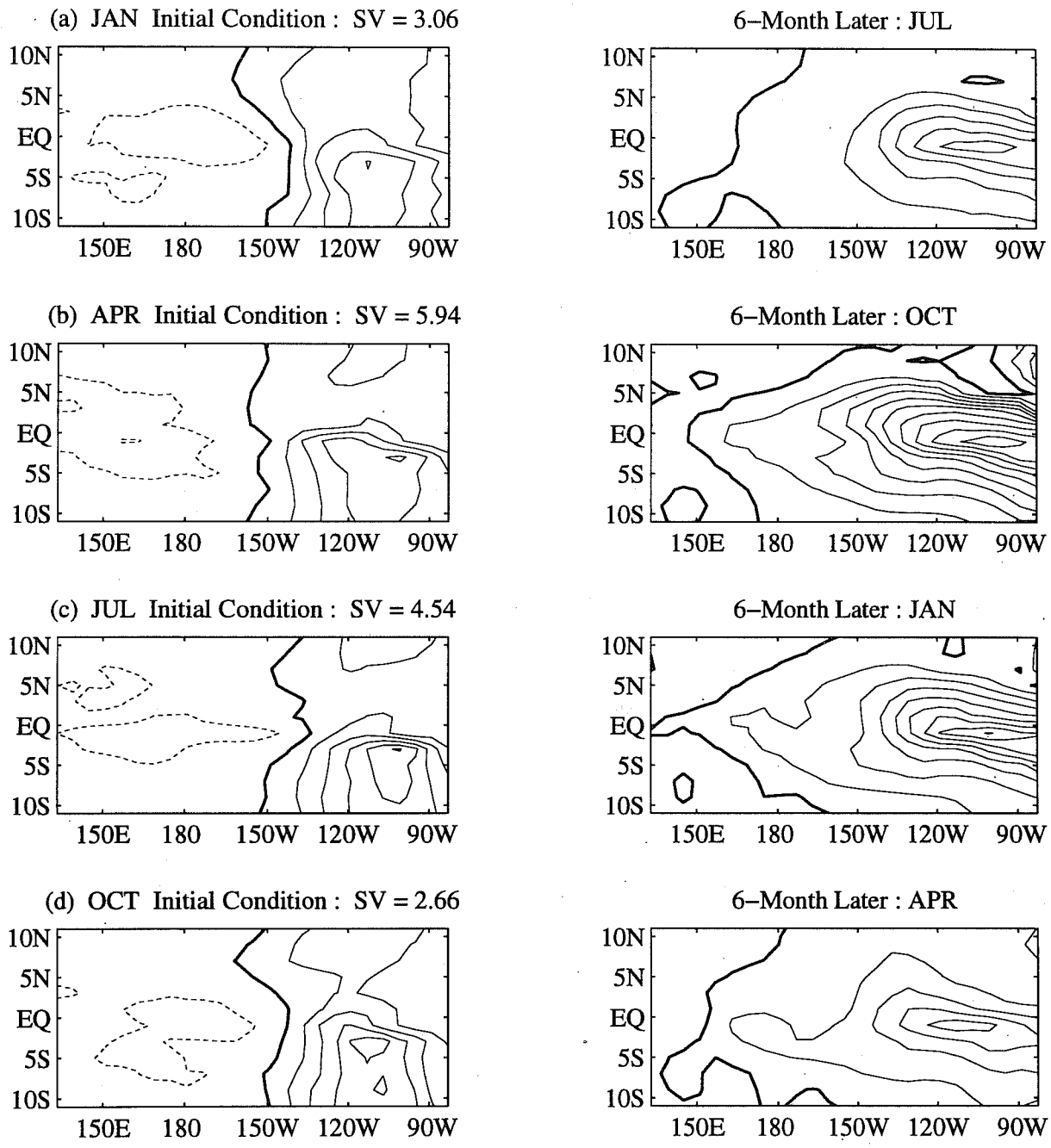

Figure 3.11: SST associated with dominant 6-month singular vector at initial (left) and final (right) time, for a) January, b) April, c) July, d) October starts. The basic state trajectory is a climatological annual cycle. From Chen *et al* (1996).

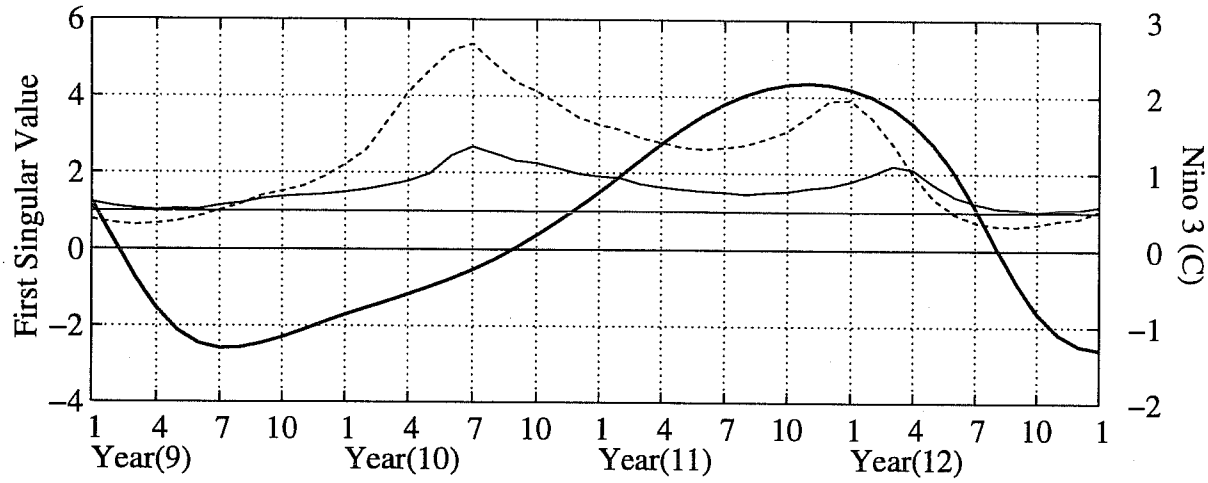

Figure 3.12: Dominant singular values for 3-month (light solid) and 6-month (dashed) from the Battisti intermediate coupled ocean atmosphere model. The basic state trajectory is a free integration of the model without climatological annual cycle. The NINO3 index from the basic state trajectory is shown as the heavy solid line. From Chen *et al* (1996).

Of course, in keeping with the other results discussed in this section, it is likely that these singular vectors will depend on the state of ENSO itself, as well as on the annual cycle. In order to understand this further, singular vectors have been calculated with respect to a 'free trajectory' of the Battisti model which includes ENSO variability but (for this integration in particular) has no annual cycle. In fact, when the Battisti model is run freely, the extrema of the model (NINO3) SST anomalies range from over 2C in the warm phase to less than -1C in the cold phase. The solid line in Fig 3.12 shows a timeseries of Nino 3 SST anomaly from year 9- year 12 of a model climate integration. Also shown are the dominant 3- and 6- month singular values associated with singular vector calculations made using this freely evolving basic state. It can be seen that the growth rates do indeed depend on the state of ENSO in the basic state trajectory. For example, largest growth occurs during the transition phase between the cold and warm event. A secondary maximum is associated with the trajectory portion starting near the peak of the warm event.

The dependence of the dominant singular value on ENSO is of relevance when we consider the decadal variability of ENSO predictability. In particular, as discussed by Balmadesa *et al* (1995), the 'spring barrier' effect is more prominent in the 1970s than in the 1980s. In order to study whether there is any decadal variability in the dominant ENSO singular values, Y-Q. Chen (personal communication, 1995) has estimated the mean and standard deviation of the dominant singular values over the periods 1960-1975 and 1975-1990 respectively. Results indicate that there is a less significant annual cycle in the dominant singular values in the period 1975-1990 than in the period 1960-1975. This is consistent with the fact that ENSO itself was more active in the latter period.

4 PREDICTABILITY OF THE SECOND KIND.

4.1 Uncertainty in forcing

In section 2, initial value problems were referred to as predictions of the first kind. In a prediction of the second kind, we estimate how (the attractor of) a given dynamical system responds to a change in some prescribed parameter or variable. The response of climate to doubling CO_2, or of the stratosphere to an increase in CFCs, or of an atmospheric GCM to a prescribed change in SST, are all predictions of the second kind. Uncertainties in such predictions may arise from the accuracy in the prescribed change itself, or from uncertainties in model formulation. (In practice, of course, many forecasts do not fall exclusively into either of these two categories).

Even though predictions of the second kind are, by construction, not sensitive to initial conditions, the underlying instabilities of the flow play an important role in determining the associated predictability. To see this, let us apply the singular vector analysis discussed in section 2 to a forced problem. Consider then the generalisation of (2.2) to

$$\frac{d\mathbf{x}}{dt} = \mathbf{M}_l\mathbf{x} + \mathbf{f}(t) \tag{4.1}$$

As before, we let us integrate this equation over the finite time interval $[t_1, t_0]$. Using the tangent propagator $\mathbf{L}(t, t_0)$ (*cf* equation 2.3), then the solution to (4.1) can be written as

$$\mathbf{x}(t_1) = \mathbf{L}(t_1, t_0)\mathbf{x}(t_0) + \int_{t_0}^{t_1} \mathbf{L}(t_1, s)\mathbf{f}(s)ds \tag{4.2}$$

From (4.2) it can be seen that the effect of an initial error $\mathbf{x}(t_0)$ can be replicated by the action of the impulsive forcing $\mathbf{f}(t) = \mathbf{x}(t_0)\delta(t - t_0)$. Hence, the maximum response $||\mathbf{x}(t_1)||$ from such a normalised impulsive forcing occurs when $\mathbf{f}(t) = \boldsymbol{\nu}_1(t_0)\delta(t-t_0)$, where $\boldsymbol{\nu}_1(t_0)$ is the dominant singular vector at initial time associated with the interval $[t_1, t_0]$. More generally, if $\mathbf{f}(t)$ is a normalised impulsive forcing $\mathbf{f}(t) = \mathbf{x}(s)\delta(t - s)$, $t_1 < s < t_0$ then the maximum response $||\mathbf{x}(t_1)||$ can be induced by choosing $\mathbf{x}(s)$ to be the dominant initial singular vector for the interval $[t_1, s]$. Putting this together we can see that if $\mathbf{f}(t)$ is any spatially normalised forcing, then the maximum response at t_1 will be obtained by setting $\mathbf{f}(t) = \boldsymbol{\nu}_{[t_1,t]}(t)$, the dominant initial singular vector over the interval $[t_1, t]$.

Now let us interpret the forcing $\mathbf{f}(t)$ as an uncertainty in model formulation which, for the sake of argument, we shall assume arises principally from the physical parametrisations. We have argued that a complete specification of the initial state would include not only the best estimate of the initial conditions, but also a probability distribution of the error associated with that best estimate. Similarly, given the inherent uncertainties in parametrising sub-gridscale processes, a complete specification of the diabatic tendency in a grid box should include not only our best estimate of the diabatic tendency (*ie* the parametrised tendency), but also a probability distribution of the error associated with that estimate.

When considering the probability distribution of parametrised diabatic tendency, it is certainly not permissable to ignore the first moment. This first moment can be thought of as defining what is generally referred to as 'systematic error'. However, in addition to its systematic component, the parametrised diabatic tendency will certainly have a stochastic component of error. Consider, for example, the parametrisation of convective heating in terms, say, of resolved moisture fluxes or temperature profiles. If convectively-driven mesoscale circulations occur on scales which are not substantially smaller than the

resolution of the model, then the usual assumptions of a quasi-equilibrium of convective heating elements within a grid box will fail. This failure will generate a second moment of the PDF.

The basic message behind (4.2) is that the system response to forcing errors depends very much on the convolution of this forcing with the dynamical instabilities of the flow itself. This can be seen clearly if we put $\mathbf{f}(s) = \mathbf{f}_0$, $\mathbf{x}(t_0) = 0$ so that

$$\mathbf{x}(t_1) = \mathcal{L}(t_1, t_0)\mathbf{f}_0 \tag{4.3}$$

where

$$\mathcal{L}(t_1, t_0) = \int_{t_0}^{t_1} \mathbf{L}(t_1, s)ds \tag{4.4}$$

4.2 A simple chaotic model paradigm for predictability of the second kind

As a simple example of the impact of a fixed forcing on a heterogeneous attractor, consider the Lorenz (1963a) model

$$\begin{aligned} \dot{X} &= -\sigma X + \sigma Y \\ \dot{Y} &= -XZ + rX - Y \\ \dot{Z} &= XY - bZ \end{aligned} \tag{4.5}$$

Singular values for the Lorenz model have been computed by a number of authors (*eg* Mukougawa *et al*, 1991; Abarbanel *et al*, 1991; Trevisan, 1993). Fig 4.1 shows the distribution of exponents of dominant singular values for two choices of the trajectory length. For relatively long trajectory portions, the distribution of singular values (expressed as an equivalent exponent) is relatively narrow and is clearly asymptoting to the appropriate largest Lyapunov exponent (here about 1.5). For short trajectory portions the distribution of maximum exponents is broad, varying from negative values (*ie* decaying singular vectors) to values over one order of magnitude greater than the fastest growing Lyapunov exponent.

Let us now examine some time traces of one of the state variables of the modified Lorenz model

$$\begin{aligned} \dot{X} &= -\sigma X + \sigma Y + f_0 \\ \dot{Y} &= -XZ + rX - Y + f_0 \\ \dot{Z} &= XY - bZ \end{aligned} \tag{4.6}$$

as the time invariant forcing f_0 increases from zero (see Fig 4.2). Notice that the X values do not simply translate to larger values as f_0 increases, rather the probability that the state vector resides in the regime with positive X increases, and the probability that the state vector resides in the regime with negative X decreases. The X-values of the regimes themselves are largely unchanged.

Fig 4.3a shows the state vector PDF of the Lorenz model (4.5) computed from a long integration. It is effectively symmetric with maxima corresponding to the centroids of the butterfly-wing regimes. Fig 4.3b shows the PDF of (4.6) with non-zero f_0; the PDF is now biased to one of the regimes; however, the phase space position of the regime centroids remains essentially unchanged.

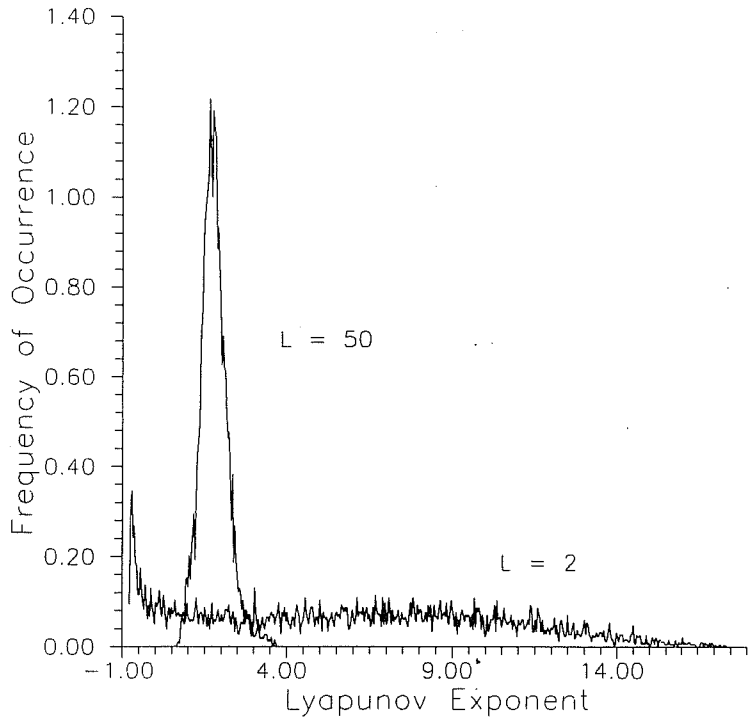

Figure 4.1: The distribution of the largest singular value,σ, (shown as its exponent $\ln \sigma$) for the Lorenz model (4.5) for two trajectory lengths L (L=50, L=2). Each distribution is normalised to unity. From Abarbanel *et al* (1991).

This behaviour can be understood in terms of the heterogeneity of finite-time singular values on the attractor. In particular, at the regime centroids (PDF maxima for the state vector time averaged over the fast oscillation time scale) the singular values are rather small, corresponding to the fact that the attractor is rather stable in this part of phase space. On the other hand, in other parts of the attractor, particularly near the origin, the singular values are particularly large, corresponding to a very unstable saddle point instability. In the Lorenz model (4.5), the outset (*eg* Thompson and Stewart, 1991) of the saddle is symmetric with respect to the two Lorenz regimes. In the modified model (3.2) it becomes biased towards one of the regimes.

A statement of these results in general terms leads to the following nonlinear paradigm (Palmer, 1993). The *influence* of a weak forcing f_0 on a nonlinear system (such as the climate) is greatest in regions of phase-space where the dominant singular value is large. On the other hand, the *response* of the system to f_0 is greatest in regions where the local PDF is a maximum, and singular values are small. To first order, the response to f_0 will be a change in the value of the PDF at the maxima.

This analysis is broadly consistent with recent studies of systematic errors in weather prediction and climate models. For example, as shown by Molteni and Tibaldi (1990), medium-range systematic errors tend to have large-scale equivalent barotropic structures which correspond reasonably well with the regime structures discussed in section 2. In order to understand how such errors arise, *ie* what systematic forcing errors these structures are most sensitive to, we need to estimate either a pseudo-inverse or a sensitivity gradient of that error pattern over an ensemble of trajectory portions, that, together, cover the climate attractor. Such studies are underway (see section 3.5 and section 6).

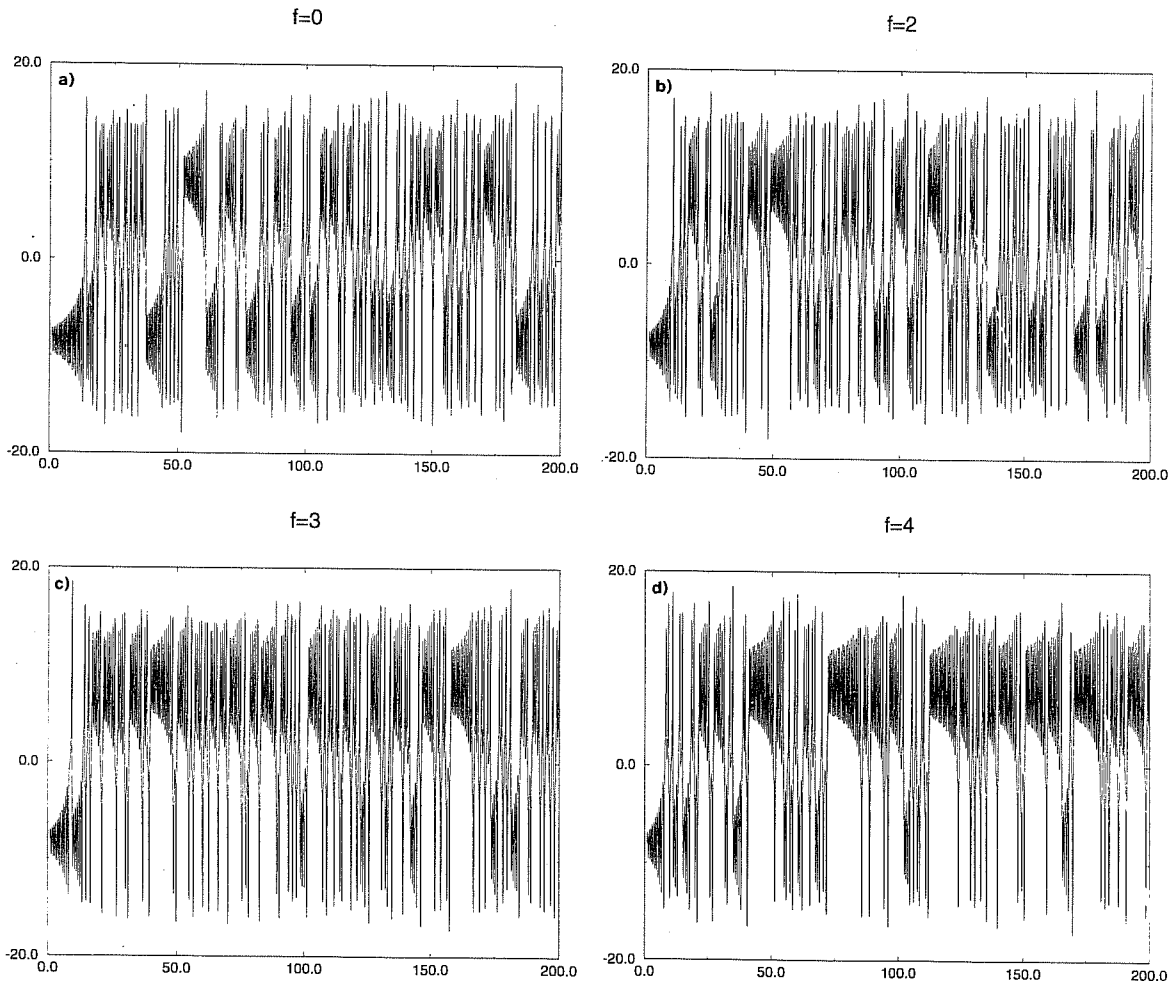

Figure 4.2: Timeseries of the X component of the modified Lorenz equation (4.6) for a) f_0=0, b) f_0=2, c) f_0=3, d) f_0=4.

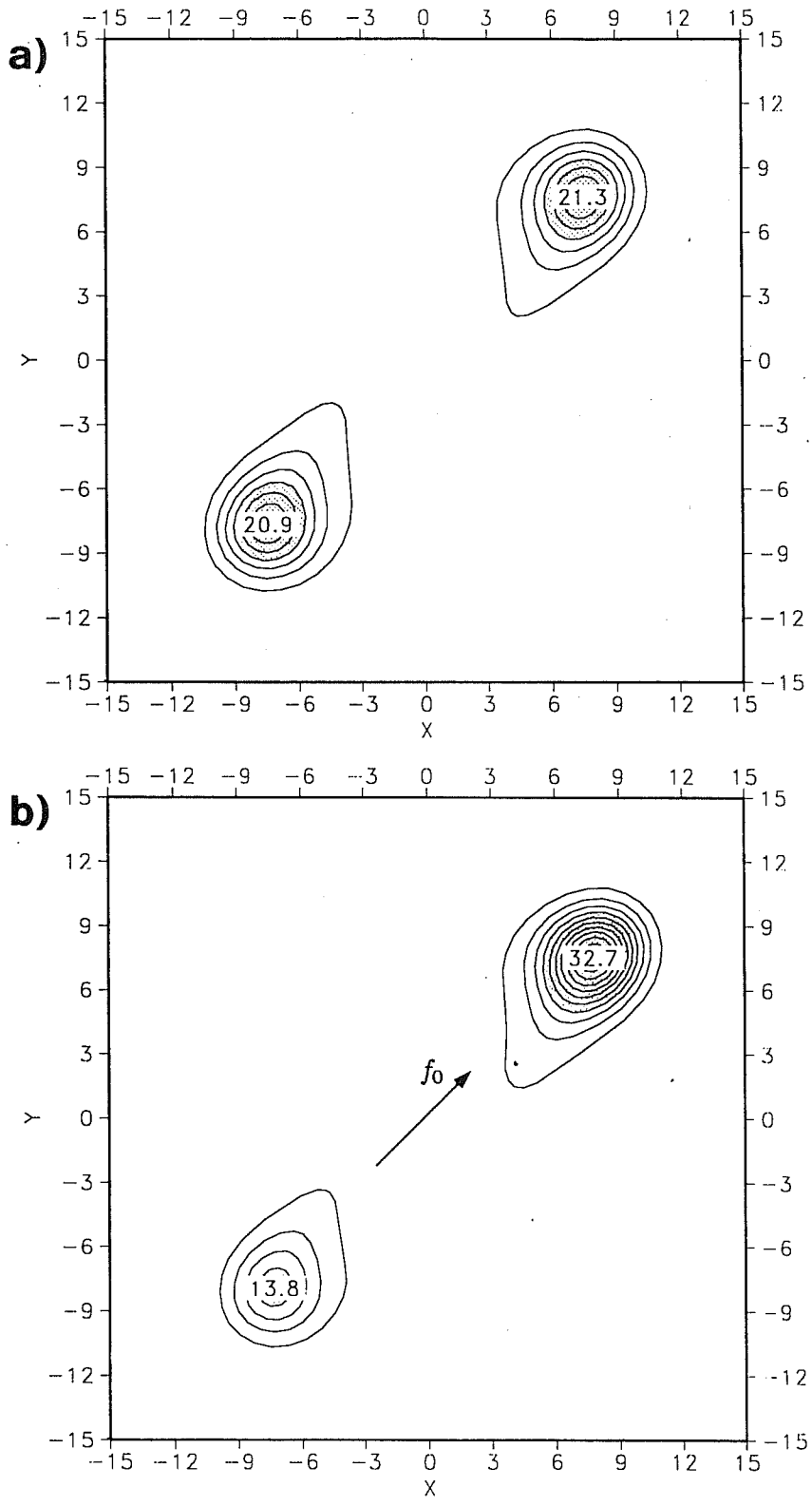

Figure 4.3: PDF of the Lorenz model in the X-Y plane, low-pass filtered to remove oscillations around a regime centroid (a) from the unforced model (b) with a constant f_0.

It should be noted that this paradigm is very hard to prove from first principles; even the notion of existence and uniqueness of a PDF is hard to establish. Nevertheless below we shall use the paradigm as a possible means of interpreting climate variability.

4.3 Application to atmospheric forcing by tropical SST anomalies

Up to now I have imagined f_0 to represent a model uncertainty. However, we can apply the paradigm more generally. Consider a prediction of the second kind, mentioned earlier; the response of an atmospheric GCM to imposed SSTs. Fig 4.4 a,b shows the 1000hPa temperature and 500hPa height difference in the wintertime climate of (a recent version of) the ECMWF model using firstly SSTs from the El Niño winter 1986/87, and secondly using SSTs for the winter 1988/89.

Applying the nonlinear paradigm, the forcing associated with the imposed SST changes will have increased certain atmospheric regimes, and decreased others. Fig 4.4c shows the impact of the SST changes on the climatic frequency of the Molteni *et al* (1990) regimes. These frequency statistics have been based on 5-day mean 500hPa height fields. It can be seen, comparing 1988/89 with 1986/87, that the frequency of both clusters 1 and 2 have decreased, and the frequency of cluster 5 has increased. This change in frequency corresponds to what actually occurred.

Note from Fig 4.4a, the 1000hPa high latitude zonal mean temperature difference is positive. The reason for this is not that the SST forcing has a high latitude zonal mean positive component, it is that the temperature difference reflects the change in frequency of the cluster 2 and 5 regimes. We will return to this basic idea in section 6.

Fig 4.5b shows the time-mean 200hPa response of the UKMO GCM to a relatively small warm SST anomaly in the western Pacific, as shown in Fig 4.5a. Again, there is a PNA like response in the northern hemisphere. It can easily be seen that this response would also have significant projection onto the Molteni *et al* regimes.

However, why should the imposed west Pacific SST differences have changed the frequencies of the Molteni *et al* regimes so effectively? Now Fig 4.6a shows the dominant stationary eigenmode of the time-averaged climatological flow in a barotropic model (from Zhang, 1988). Fig 4.6b shows the adjoint of this eigenmode. As discussed in section 2, these can be thought of as final and initial singular vectors (respectively) for an indefinitely long trajectory, in the approximation where we treat the trajectory as stationary (see remarks above on the relationship between this approximation and the barotropic model approximation). The eigenmode structure (very roughly) approximates the difference field between cluster 5 and cluster 2 (having a negative PNA index). The adjoint eigenvector has no correspondence to the eigenmode itself, but rather has most of its structure in the tropics and subtropics, over Indonesia, south-east Asia and the Indian Ocean.

From this perspective, the PDFs of the dominant extratropical regimes may be most sensitive to external forcing from the tropical western Pacific area.

A second application of the nonlinear paradigm concerns the predictability of the monsoons. As discussed in Palmer (1994), the break and active phase of the Asian summer monsoon can be thought of as representing regional flow regimes in which the ITCZ has a predominantly oceanic or continental position. Intraseasonal monsoon variability can be thought of as comprising essentially chaotic fluctuations between these regimes. During warm-phase ENSO years, the PDF of the oceanic regime is enhanced leading to a greater probability of a poor overall monsoon. During cold-phase ENSO years the PDF of the continental regime is favoured, leading to greater probability of a good monsoon. In this

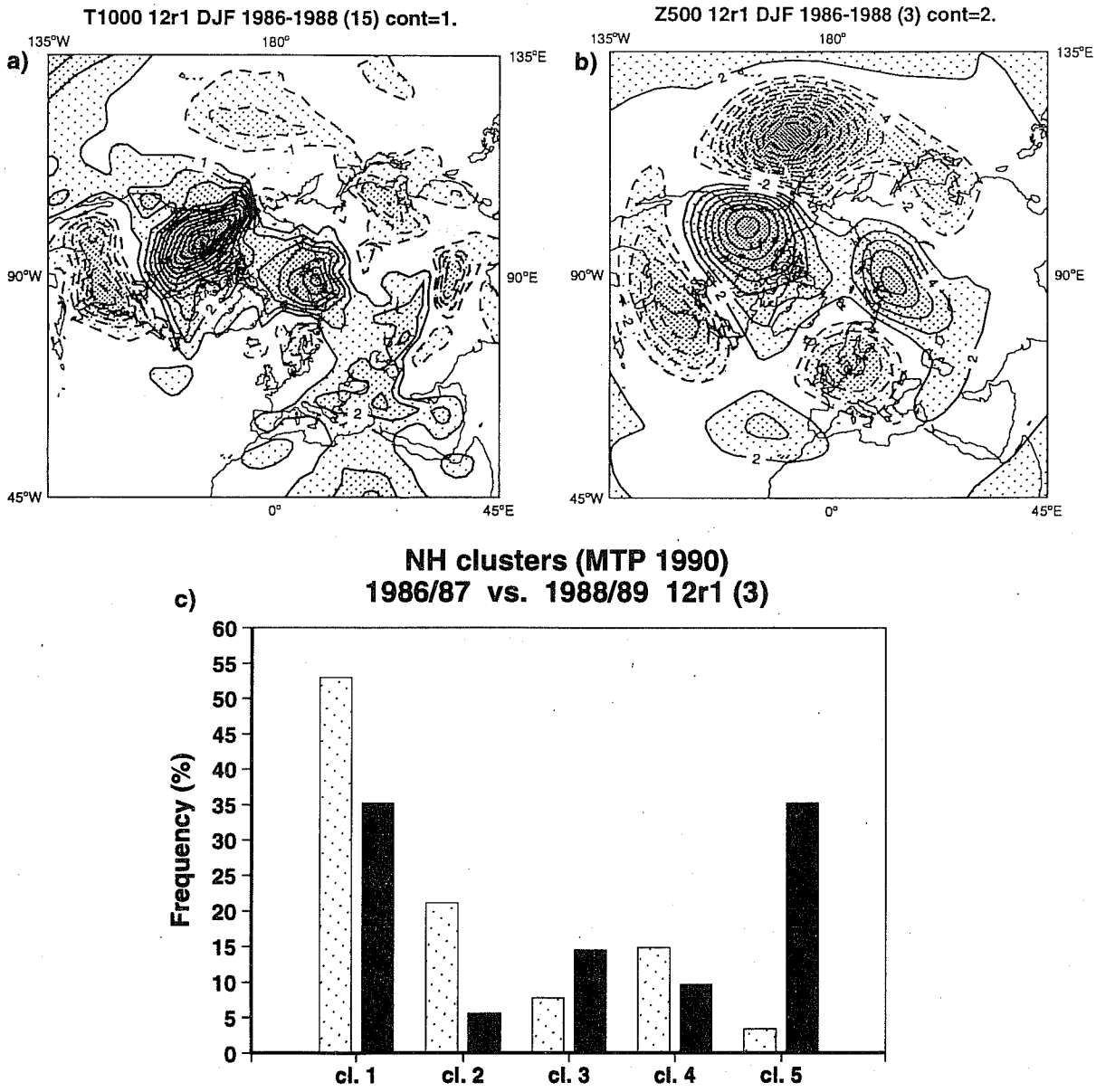

Figure 4.4: a), b) Difference between DJF 1000hPa temperature and 500hPa height (respectively) from two (3-member) 120-day ensembles of the T63L19 ECWMF atmosphere model. The first ensemble was run with observed SSTs for the winter 1986/87, the second ensemble was run with observed SSTs for the winter 1988/89. c) Cluster frequency of pentad fields with the DJF period for 1986/87 ensemble (left hand bars) and 1988/89 ensemble (right hand bars). Clusters are based on Molteni *et al* (1990) analysis.

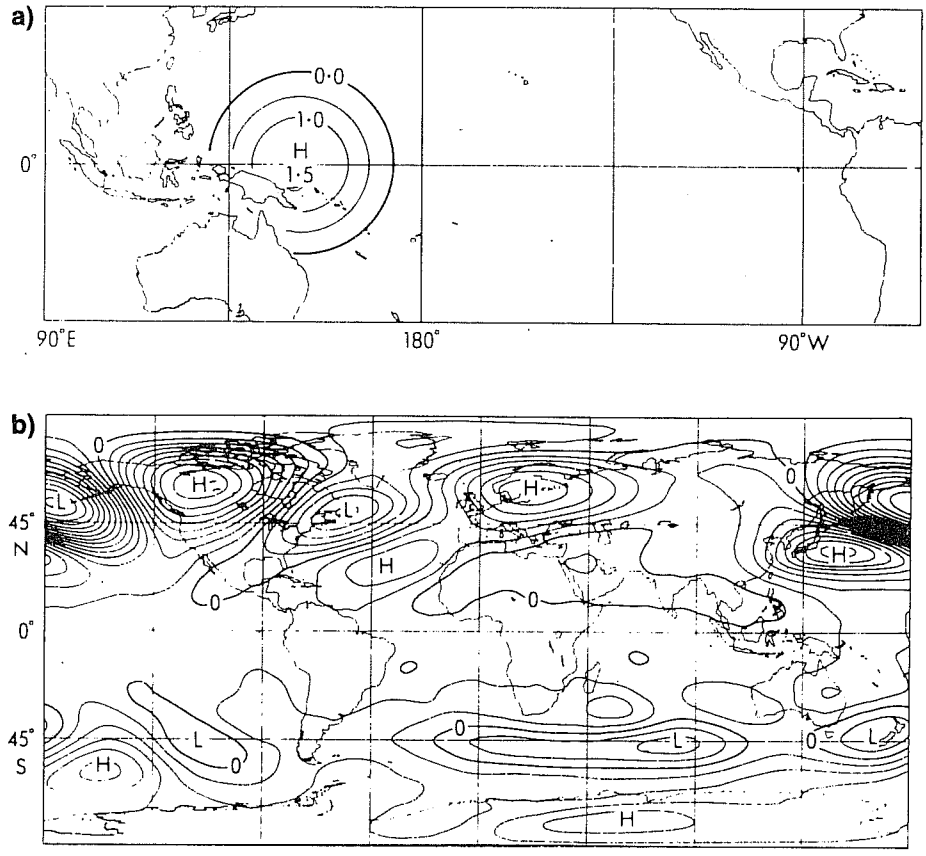

Figure 4.5: a) Idealised West Pacific SST anomaly. b) 200hPa height response of the UKMO GCM to the imposed anomaly in a). Contour interval 2 dam. From Palmer and Mansfield (1986).

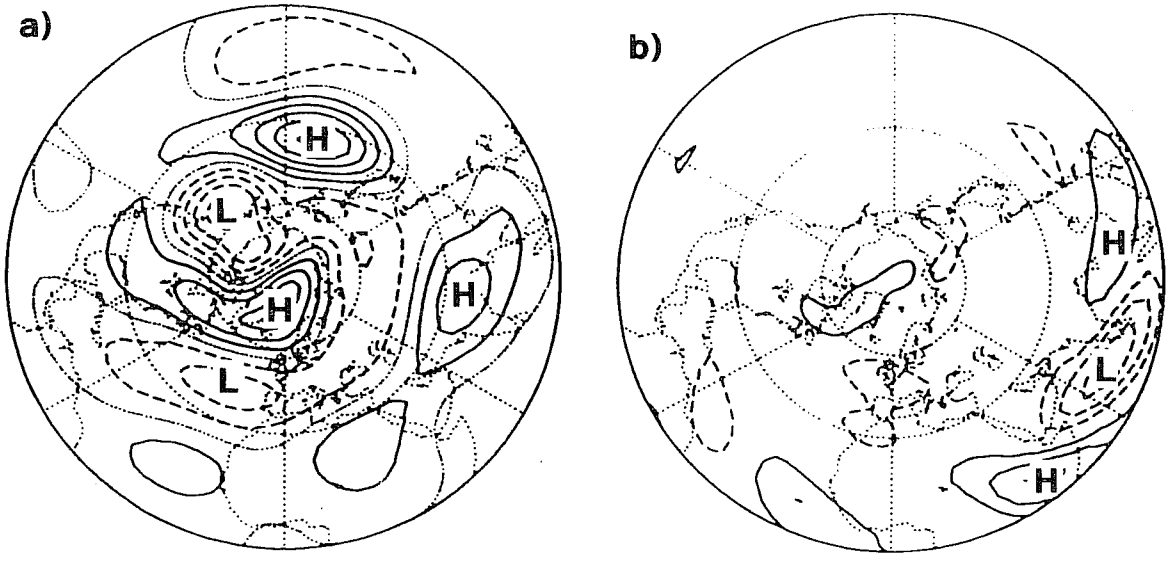

Figure 4.6: a) Streamfunction of dominant stationary barotropic eigenmode based on climatological winter mean basic state. b) Streamfunction of adjoint of the eigenmode shown in a). From Zhang (1988).

picture, the predictability of seasonal-mean monsoon fluctuations to imposed external SST anomalies is only partial, a result demonstrated in GCM ensemble integrations (Sperber and Palmer, 1996).

One simple consequence of the picture put forward is that if the circulation patterns are dominated by a few basic regimes, and if the system basically responds to weak forcing through changes in regime frequency, then the EOFs of the system will match the patterns of these regimes no matter how long a timescale they are computed over. Hence, the fact that the PNA and NAO patterns emerge as dominant EOFs on weekly, seasonal, and multi-decadal timescales is entirely consistent with the nonlinear paradigm put forward here.

We will return to the paradigm put forward here in section 6 when we discuss climate change.

5 PREDICTABILITY OF INTERDECADAL FLUCTUATIONS

5.1 Internal atmospheric variability

A basic theme underlying this paper is the chaotic nature of climate. Much of this derives from the atmosphere. The ubiquitous growth of atmospheric perturbations, as revealed by singular vector analysis above, together with the underlying nonlinear structure of the atmosphere, suggested, for example, by potential vorticity diagnosis, (*eg* the wave-breaking and wave, mean-flow interaction processes illustrated in Hoskins *et al*, 1985), is itself supporting evidence of chaotic variability.

Since chaotic processes are inherently aperiodic, a spectral analysis of a chaotic time series will reveal power over a range of timescales, possibly strongly removed from the principal timescale of the dominant instability process (Lyapunov exponent timescale). For the atmosphere, it is possible that chaotic variability associated with the 'fast' baroclinic timescale, together with the 'medium' timescale processes associated with regime dynamics, may generate a significant component of 'long' timescale, interannual and interdecadal fluctuations. One could define the word 'significant' through an f-test, comparing the fraction of low-frequency variance explained by internal atmospheric chaotic dynamics, with the fraction of variance explained by 'external' forcing (*eg* from the ocean). From a practical point of view, if chaotic variations are significant, then the predictability of the atmosphere will be limited on these timescales.

Simple model estimates (*eg* James and James, 1989) suggest that internal chaotic processes could be significant even on decadal timescales. In order to be able to have a more quantitative estimate, one needs to resort to more comprehensive models. To start to address these questions I will show results from some decadal timescale integrations made using the UKMO unified model (D. Rowell, personal communication). These integrations were made as part of a coordinated study using a number of GCMs worldwide. Results are based on an ensemble of 6 integrations in which the model was run for 45 years with observed prescribed SSTs from 1948-1993 using the UKMO GISST (Folland and Rowell, 1995) data set. The ensemble members differ only in terms of their initial conditions.

Figs 5.1 and 5.2 show the percentage of variance of simulated surface pressure that can be attributed to the time-varying SSTs for seasonal and decadal averages. This diagnostic was estimated by taking the ratio of the temporal variance of the ensemble-mean fields, to the total variance of all surface pressure fields within the ensemble. The temporal variance of the ensemble mean is assumed to be attributable to the underlying SST variability, hence in regions where the ratio is large, we can assume that the influence of

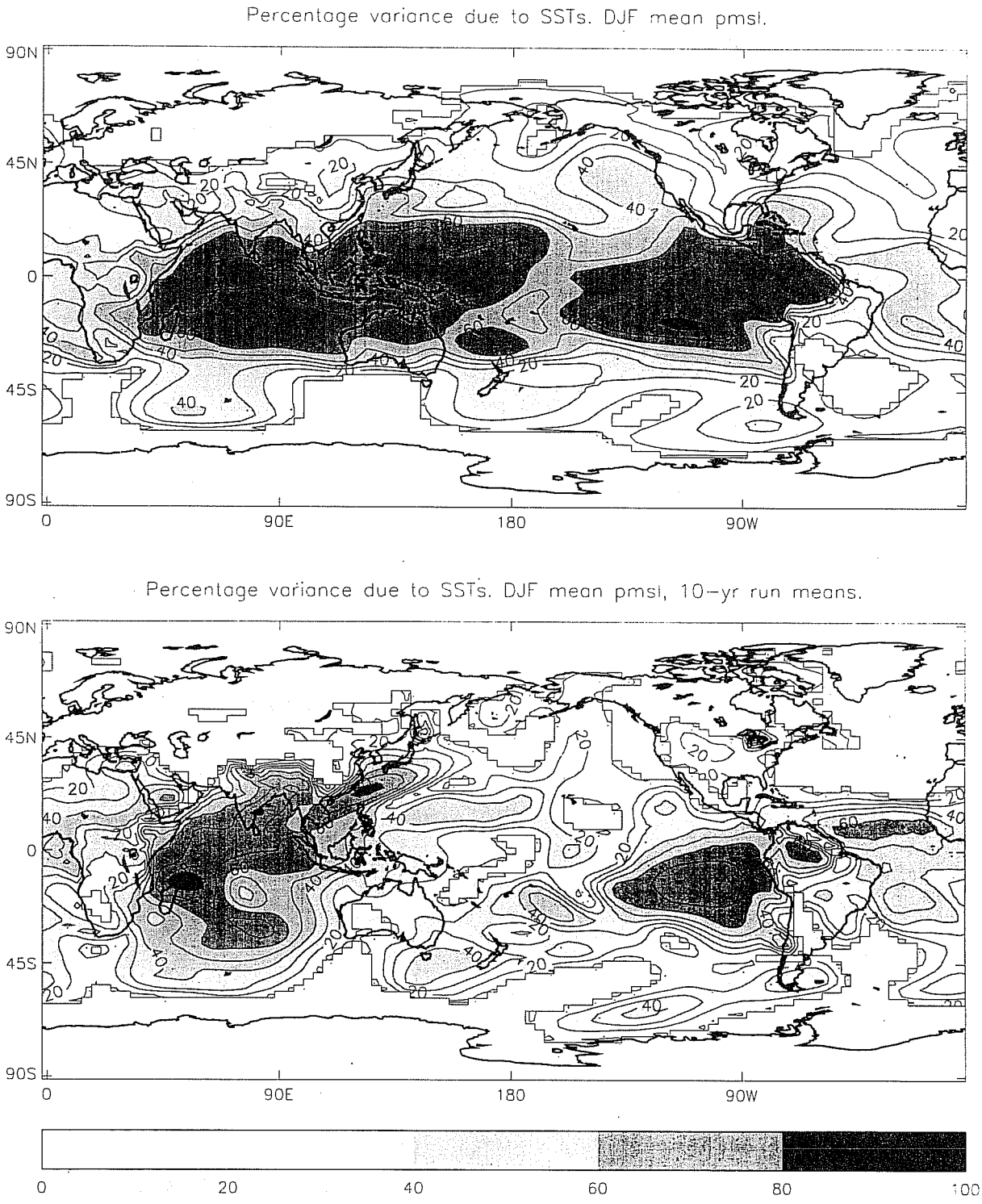

Figure 5.1: Percentage of variance for DJF due to SSTs based on analysis of surface pressure from a 6-member ensemble of 45-year integrations of the UKMO GCM made with observed specified SSTs. Top panels : seasonal mean fields. Bottom panels: running 10-year average of seasonal mean fields. (D. Rowell, personal communication).

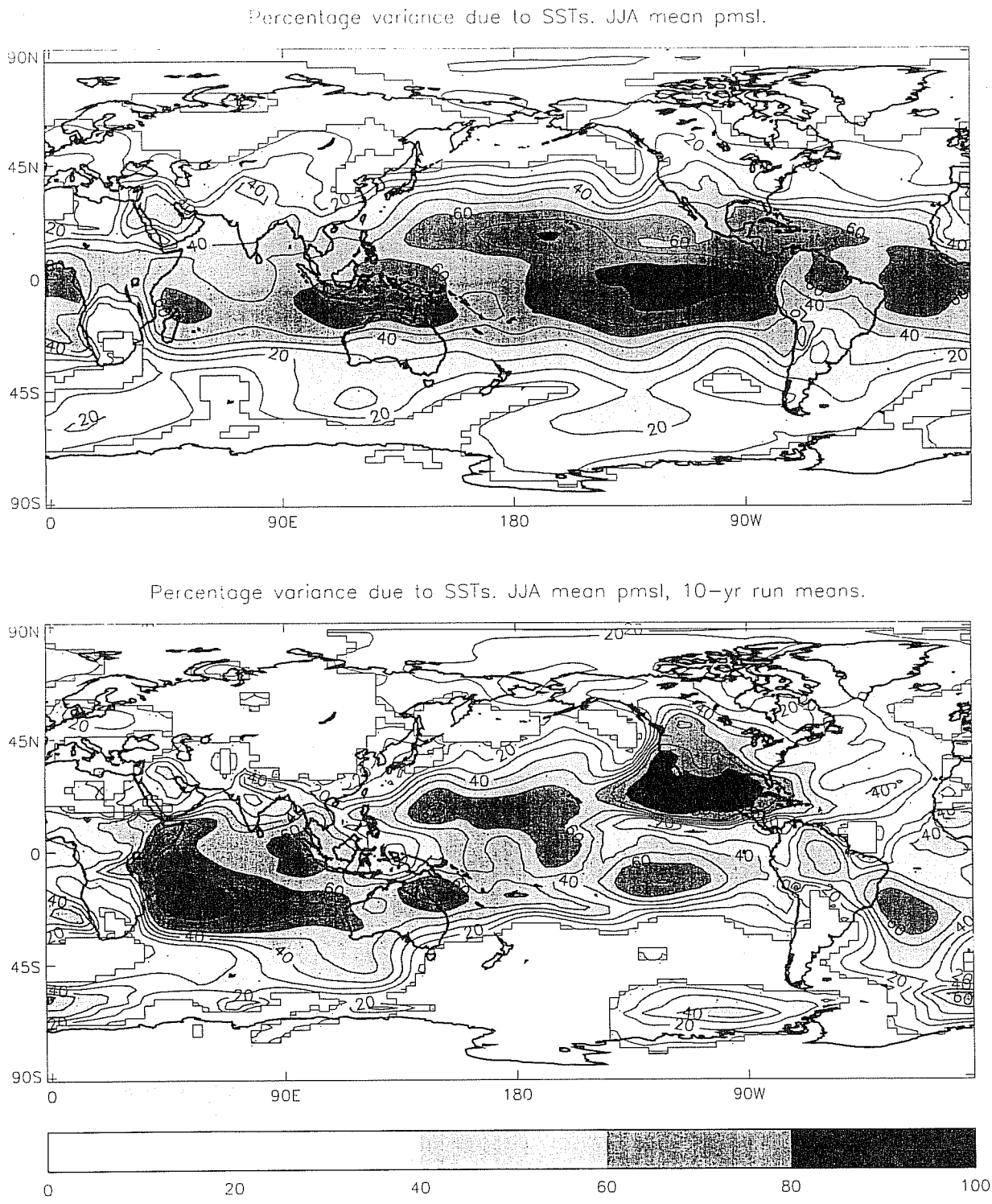

Figure 5.2: As fig 5.1 but for JJA.

time-varying SST dominates over internal atmospheric variability. Figs 5.1 and 5.2 show results for DJF and JJA respectively. For each figure the top panel shows results for inter-annual fluctuations (*ie* seasonal means), the bottom panel shows results for interdecadal fluctuations (*ie* based on 10-year running means of a given season).

Results for seasonal timescale fluctuations are consistent with many previous studies. In particular, over much of the tropics, the total ensemble variance is dominated by the effects of SST variability, whilst in the (more chaotic) extratropics the percentage is generally smaller. In the extratropics, the maximum percentage occurs over the north-east Pacific and is probably associated with the PNA response to El Niño SST anomalies. In summer, the percentage of variance in the north Pacific is smaller, consistent with a reduction in tropical-extratropical teleconnectivity associated with weak potential vorticity gradients.

Interestingly, the percentage of variance of the decadal fluctuations explained by SST variability is, in many areas, smaller than that associated with seasonal fluctuations. In winter, for example, there are localised regions over the Indian Ocean, eastern Pacific, tropical Atlantic and so on, where the percentage of variance exceeds 60%, but in other areas, such as the north Atlantic, it appears negligible. This latter result might cause surprise to some people, given the debate about the role of the thermohaline circulation on atmospheric decadal variability. In summer, the percentage of SST-explained variance of decadal fluctuations is somewhat larger in the extratropics. Of course, one has to bear in mind that these results have been obtained by integrating with SSTs over a specific 45 year period.

5.2 The role of the oceans on decadal predictability

Although the results in Figs 5.1 and 5.2 suggest that internal atmospheric dynamics can explain a considerable amount of the observed decadal variability (especially in winter), there is modelling evidence that ocean dynamics might enhance the amplitude of decadal fluctuations. For example, Manabe and Stouffer (1996), have studied the geographical distribution of the standard deviation of 25-year mean surface air temperature from 1000 year integrations of three different models: a coupled GCM, an atmospheric GCM coupled to a ocean mixed layer model, and an atmospheric GCM with fixed SSTs. Results show that over continents, the standard deviations in all three runs are broadly comparable. Over much of the oceanic regions, the coupled and mixed layer models produce comparable standard deviations which in turn are larger than the fixed SST run. Over specific regions such as the Denmark Strait and in some regions over the circumpolar ocean of the Southern Hemisphere, the standard deviation of the coupled model is larger than the mixed layer model.

There are in fact reasons to suspect that the influence of the oceans on the atmosphere may be somewhat larger than suggested in Manabe and Stouffer (1996) analyses. In particular, if the feedback from the transient eddies onto the mean flow is an essential component in accounting for the impact of mid-latitude SSTs on the atmospheric flow (see below), then this impact might be under-represented in a model in which the transient eddy covariances were weak. It is known that low-resolution GCMs, and the R15 GFDL GCM in particular (Held and Phillipps, 1993) does suffer from excessively weak eddy momentum fluxes. Secondly, if eddy-mean-flow interaction is important, then if observed SST anomalies are added to a model in which the storm track position has systematic error, the potential impact of midlatitude SST anomalies may be underestimated. In fact significant interdecadal midlatitude air-sea interaction has been found in a coupled

GCM integration by Latif and Barnett (1994). In this case, the atmosphere model was integrated at T42 resolution, and, moreover, the SST anomalies were 'in balance' with the dynamics of the overlying atmosphere model.

On the other hand, just because the ocean may contribute to decadal atmospheric variability, this does not mean that the oceanically-forced component is predictable.

For example, according to diagnosis of experiments by Palmer and Sun (1985), the atmospheric circulation can respond to prescribed midlatitude SST anomalies near the western ocean boundaries through processes which intimately involve baroclinic eddies. In broad terms, by warming SST, for example near Newfoundland, the baroclinic gradient near the climatological region of cyclogenesis is weakened, which reduces storm-track activity. Through wave-mean flow interaction processes (diagnosed using the E-vector), the mean flow over and immediately downstream of this region is weakened throughout most of the depth of the troposphere. By weakening the mean flow, the heat loss from ocean to atmosphere is reduced and the SST anomaly can be maintained. However, as simple mixed- layer ocean models suggest (*eg* Daly, 1978) if the surface wind forcing is weakened over the North Atlantic, then SSTs will warm (*cf* Bjerknes, 1964). Hence there is the possibility of a weak positive feedback between ocean and atmosphere over the north Atlantic.

The net effect of this feedback is to redden the spectrum of atmospheric variability by making atmospheric weather regimes (*eg* associated with the North Atlantic Oscillation in the case of Atlantic SSTs, the PNA pattern in the case of Pacific SSTs) somewhat more stable. However, there is no evidence from these experiments to suggest that the regime transitions are themselves any more predictable through coupling to an ocean. Indeed, if such transitions are ultimately associated with fast baroclinic processes, it is unlikely that coupling to the oceans would alter the predictability timescale of these transitions.

An initial study of coupled-model ensemble experimentation appears to support this view about decadal predictability. Fig 5.3a (from Griffies and Bryan, 1996) shows 200 year of linearly detrended anomalous yearly-averaged thermohaline circulation (THC) index from a run of the GFDL coupled model. Also shown is the time series after a 10-year low pass filter has been applied (thick solid line). Fig 5.3b (also from Griffies and Bryan, 1996) shows the THC index for a 9-member ensemble made by adding atmospheric perturbations at year 500 of the main run. Although the THC index clearly has substantial variability on multi-decadal timescales, its predictability appears to be determined by the overlying chaotic atmospheric variability, which is much shorter than the dominant THC timescale.

5.3 A simple chaotic 'coupled' model paradigm for decadal fluctuations and predictability

To explore these ideas further, I want to put forward another simple extension of the Lorenz model. As before, the basic Lorenz model (4.5) describes the atmosphere, now it is coupled to a simple ocean model, which here is simply a storage device. The 'coupled model' equations are:

$$\begin{aligned} \dot{X} &= -\sigma X + \sigma Y + \alpha \int_{-\infty}^{t} X(t') e^{-\beta(t-t')} dt' \\ \dot{Y} &= -XZ + rX - Y + \alpha \int_{-\infty}^{t} Y(t') e^{-\beta(t-t')} dt' \\ \dot{Z} &= XY - bZ \end{aligned} \tag{5.1}$$

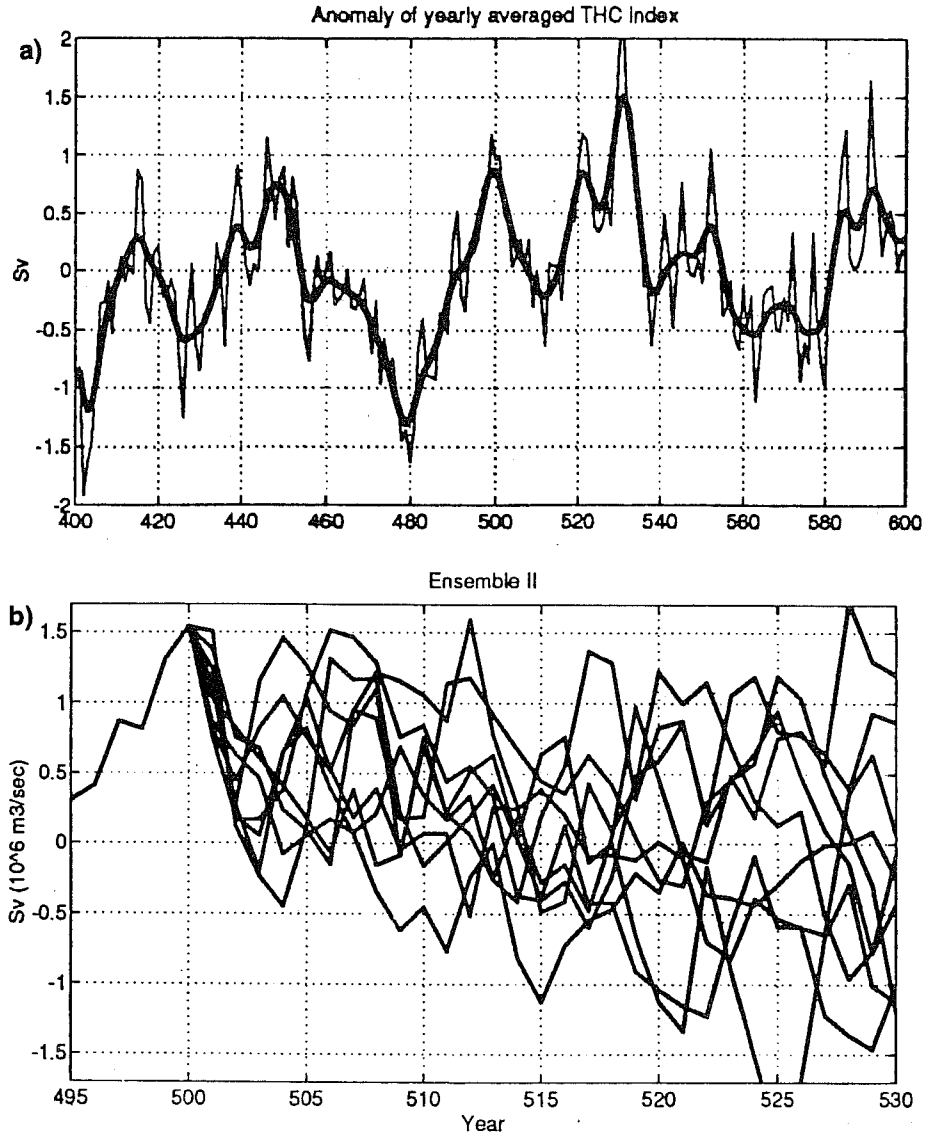

Figure 5.3: a) 200 years of linearly detrended anomalous yearly averaged thermohaline circulation index from the central portion of a coupled GCM experiment (thin solid line). The time series after a 10-year low-pass filtering has been applied is also shown (thick solid line). b) a 9-member ensemble of yearly averaged anomalous thermohaline circulation index from the coupled model. The ensemble starts from year 500 of the climatology. (From Griffies and Bryan, 1996.)

Here α and β crudely parametrise the midlatitude ocean SST and mixed-layer depth respectively. We presume that α is small, so that the storage terms do not destroy the chaotic nature of the dynamical system. If the state vector has resided in one regime of the Lorenz attractor over the period β^{-1} preceding the current time, then the storage effect will generally increase the probability that the system stays in that regime. If the state vector has made a regime transition during the time β^{-1} preceding the current time, then the storage term will have little effect on the subsequent evolution.

Interested readers can experiment for themselves by noting that (5.1) can be readily transformed into a 5th order set of ordinary differential equations by introducing two additional independent variables to represent the ocean storage terms. The (linear) dynamical equations that govern the storage variables are reminiscent of the schematic model put forward by Hasselmann (1976) for obtaining a red noise output from a stochastic white noise atmospheric input. However, unlike the Hasselmann model, the ocean is coupled to a deterministic 'atmosphere' and hence partially stabilises this atmosphere.

One interesting aspect of (5.1) is that even though β^{-1} may be just a few Lorenz time units, the storage terms can induce substantial variability on a timescale of hundreds of Lorenz time units. For example, Fig 5.4a shows a timeseries of the X component of (4.5) with a running mean of 50 Lorenz time units applied to X. It should be noted that the regime centroids are at about $X = \pm 9$. Fig 5.4b shows the same timeseries but from (5.1) (with $\alpha = 0.12, \beta = 0.3$). This reddening is found in the surface air temperature spectra in Manabe and Stouffer's (1995) study.

The intrinsic predictability of the 'coupled' model (5.1) is governed by the internal dynamics of (4.5). This can be seen in Fig 5.4c where two extra integrations are made by adding extremely small perturbations to X at t=400. The predictability timescale O(10 time units) is much shorter than the low-frequency timescale O(100 time units) apparent in Fig 5.4b. This appears to be consistent with the predictability of the THC index in Griffies and Bryan's (1996) study, shown in Fig 5.3.

It is worth noting that a model such as (5.1) could never be considered a representation of ENSO. For example, the tropical atmosphere is not, by itself, chaotic, and internal atmospheric dynamics alone cannot account for the Southern Oscillation (Dix and Hunt, 1995). Moreover, it is well known that ocean dynamics are essential for the ENSO mechanism, and therefore cannot be represented by a simple storage effect.

6 Climate change

6.1 The vertical and horizontal structure of observed climate change

In this section I would like to make some remarks about the predictability of climate change, bearing in mind the nonlinear paradigm put forward in section 4. To do this I want to focus on a very specific aspect in the validation of GCM climate change integrations. At first sight it might appear that this aspect is rather too specific for an overview discussion on predictability of climate change, but in my opinion it is symptomatic of how climate may respond to weak imposed perturbations.

The original IPCC (1990) report notes an apparent discrepancy between observations of decadal variability and GCM simulations of the impact of doubled CO_2. Fig 6.1 (reproduced from the IPCC report) shows observed temperature anomalies in the troposphere and lower stratosphere based on Angell (1988). IPCC notes that 'in the upper troposphere (300-100hPa), Fig 6.1 shows that there has been a rather steady decline in temperature

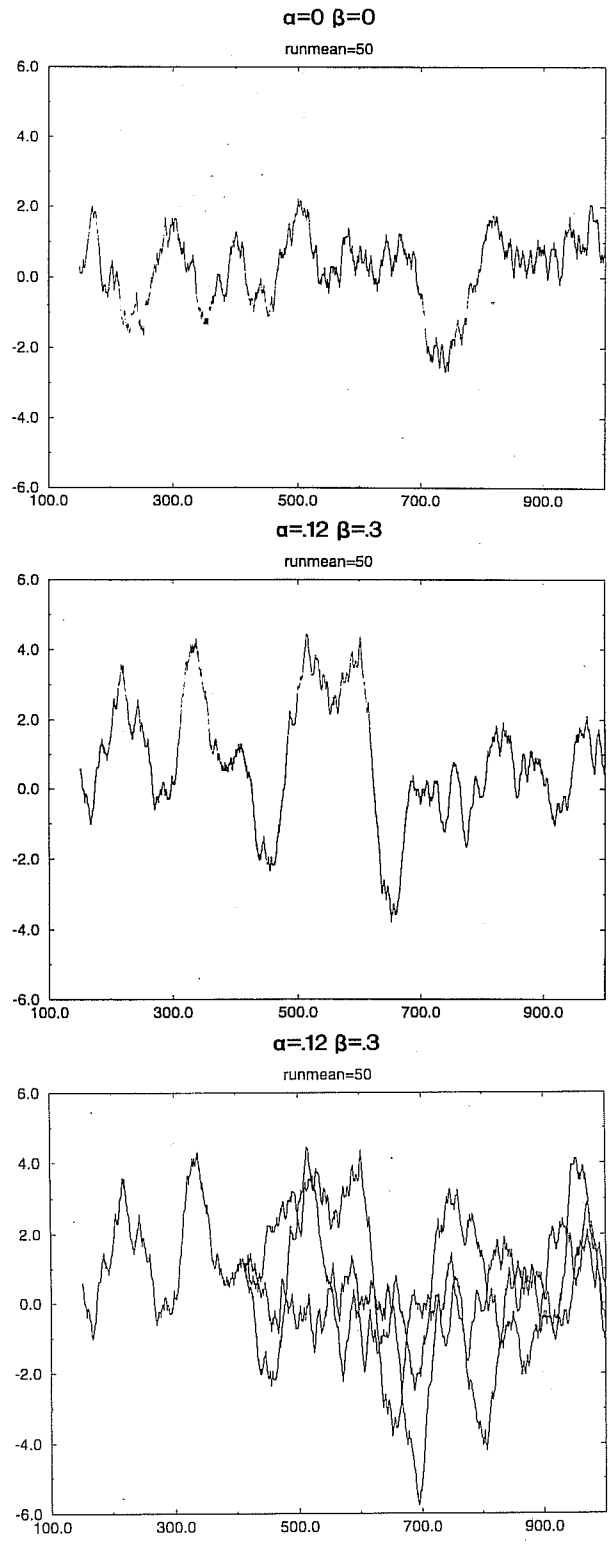

Figure 5.4: Time series of the X-component of the modified Lorenz model (5.1) with a) $\alpha = 0, \beta = 0$ b)$\alpha = 0.12, \beta = 0.3$, c) an ensemble of integrations of the Lorenz model with $\alpha = 0.12, \beta = 0.3$ in which very small perturbations are introduced at t=400.

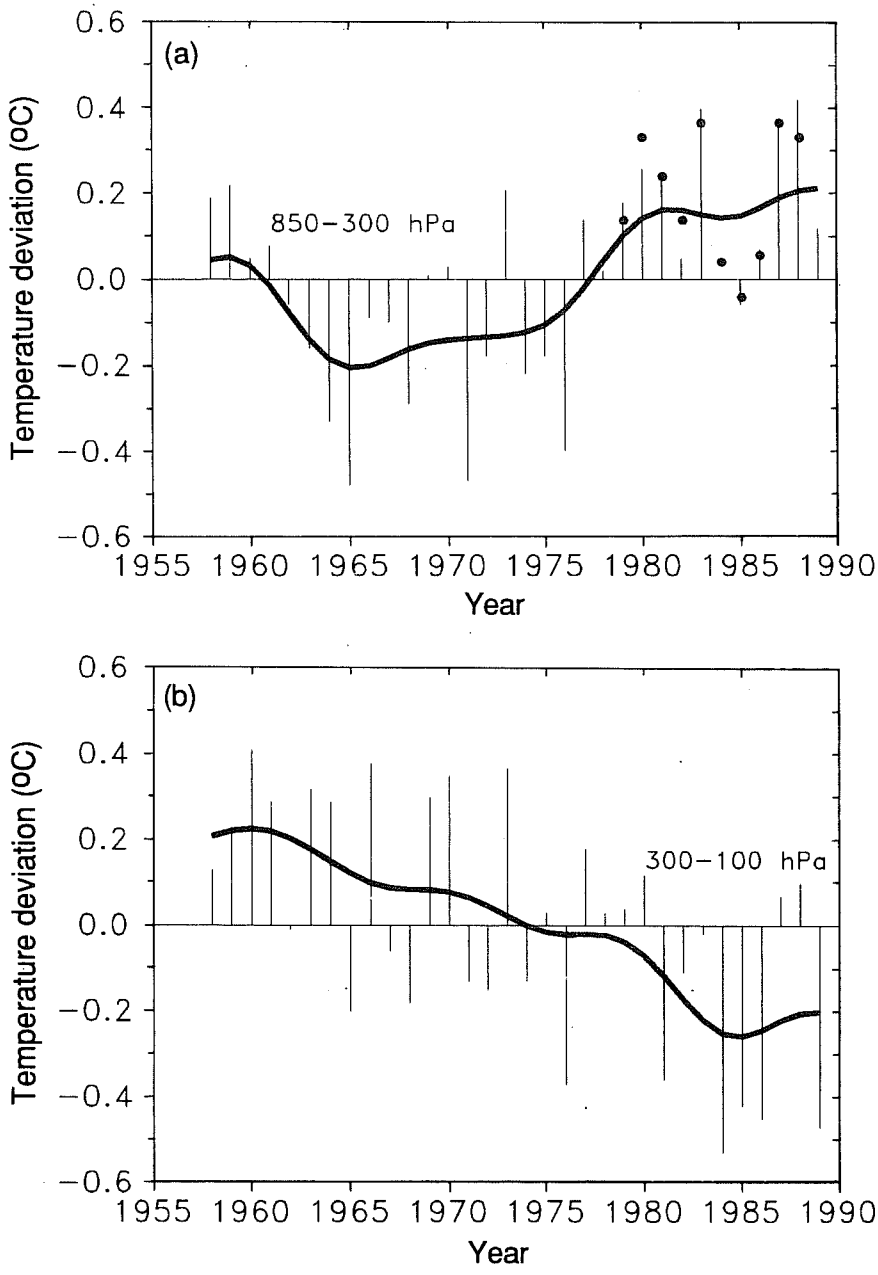

Figure 6.1: Observed temperature anomalies in the troposphere and lower stratosphere from 1958- 1989, based on Angell (1988). a) annual global values for 850-300hPa. Dots are values from Spencer and Christy (1990). b) 300-100hPa. From IPCC (1992).

since the late 1950s and early 1960s, in general disagreement with model simulations that show warming at these levels when the concentration of greenhouse gases is increased'.

To reiterate, the basic notion of the nonlinear paradigm in section 4 is that the system response to a small external forcing will, to first order, alter the residence frequency associated with naturally-occurring atmospheric regimes. Changes to the geographical structure of the regimes would be a second-order effect. This paradigm arises because the regions of phase-space in the vicinity of the regime centroids are relatively stable. The dominant instabilities are, in part, likely to be associated with saddle points of the system. An imposed time-invariant forcing would have the effect of biasing the outset of these saddles towards one or more of the regimes.

Fig 6.2 shows the geographical distribution of change in surface temperature between the 1950s and 1980s, as reported in IPCC (1992). The increase in surface temperature is largest in winter, where it is concentrated over North America and northern Eurasia, and is partially offset by cooling over the North Atlantic and the North Pacific.

The tendency for hemispheric-mean lower tropospheric temperatures to be warm during periods in which the PNA index is positive has already been noted by Gutzler *et al* (1988). For example, Fig 6.3 shows the 1000-500hPa thickness anomalies associated with the PNA 500hPa height teleconnection patterns. At the surface, the temperature anomalies associated with these thickness patterns will tend to be accentuated over land relative to the ocean, because of the smaller heat capacity of the active land surface. These positive land surface temperature anomalies will therefore dominate over the negative SST anomalies if a zonal mean temperature anomaly is calculated.

More particularly, the observed change in (northern winter) mean temperature is consistent with an increase in the frequency of the regimes shown on the left hand side of Fig 3.9, as suggested by the nonlinear paradigm outlined in section 4. One further consequence of this is that, just as the horizontal structure of decadal change should reflect the horizontal structure of the regime centroids, so also the vertical structure of decadal change should reflect the vertical structure of the regimes. Now, to some degree of approximation, the regimes themselves have an equivalent barotropic structure, with the equivalent barotropic level at about 300hPa. From the hydrostatic relationship, if there is a tendency for warming below the equivalent barotropic level, then there should be a tendency for cooling above this level. This is what Angell observes, as shown in Fig 6.1. (It can be noted that this figure is constructed from radiosonde data which has a land bias. However, according to our discussion above, most of the observed warming has occurred over land regions. Hence it is likely that, according to our nonlinear paradigm, the temperature in the upper troposphere will be cooler in a radiosonde-based estimate of hemispheric mean temperature, than in a satellite-based estimate with its more uniform coverage.)

If this interpretation of the upper tropospheric cooling is correct, then one can ask the following question.

6.2 Is the observed surface warming due to the greenhouse effect?

If the analysis in the preceeding section is correct, then the answer to this question is, in large measure, no. The greenhouse effect is a purely radiative mechanism, whilst much of the observed warming is, according to our nonlinear paradigm, the result of changes in large-scale dynamics in which certain regimes have become anomalously populated. In this picture, the warming is a property of the anomalous surface temperature associated with the regimes in Fig 3.7a,c.

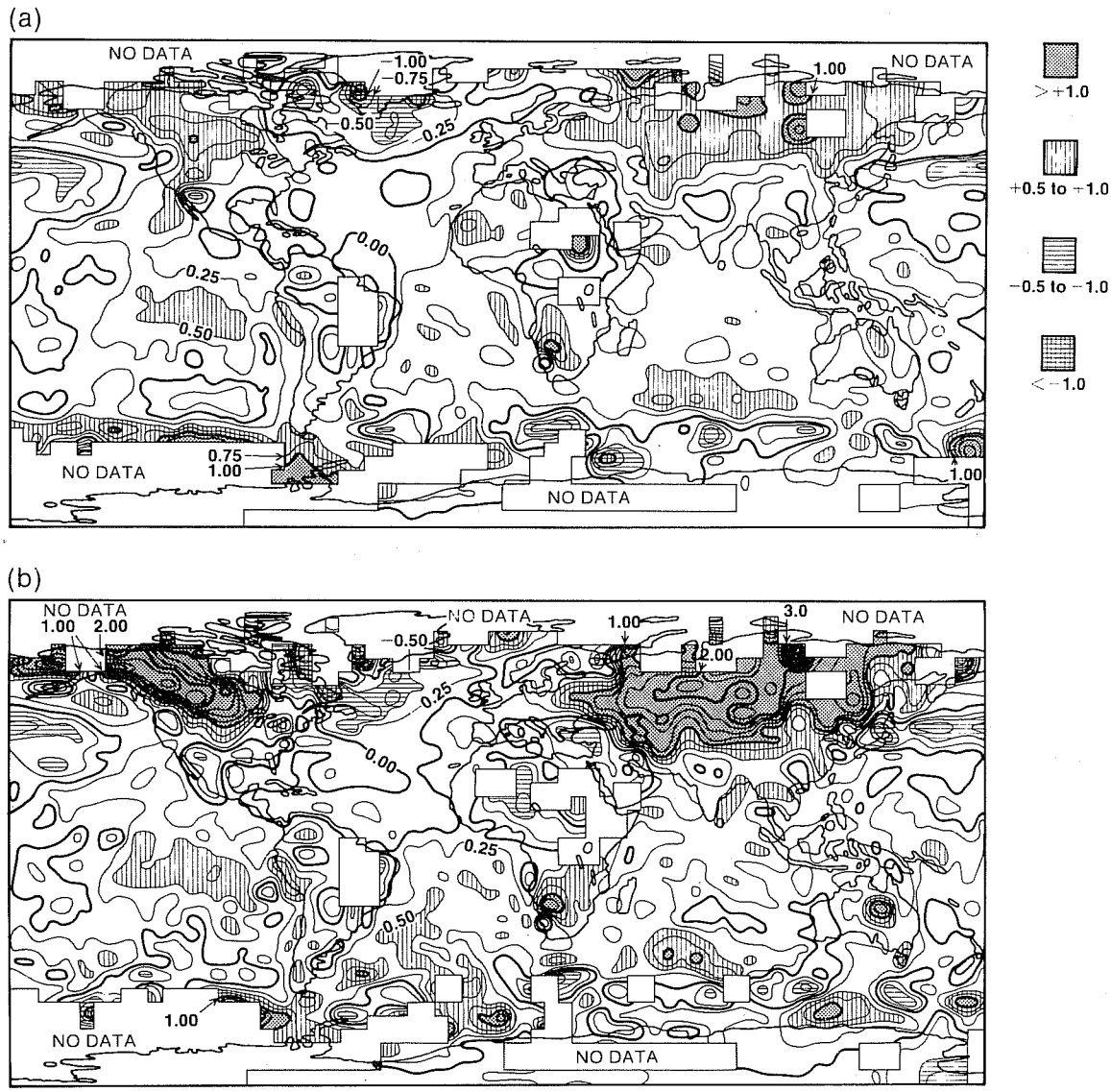

Figure 6.2: Observed surface temperature anomaly for the decade 1981-1990 relative to the 1951-80 average (a) annual average (b) winter average. From IPCC (1992).

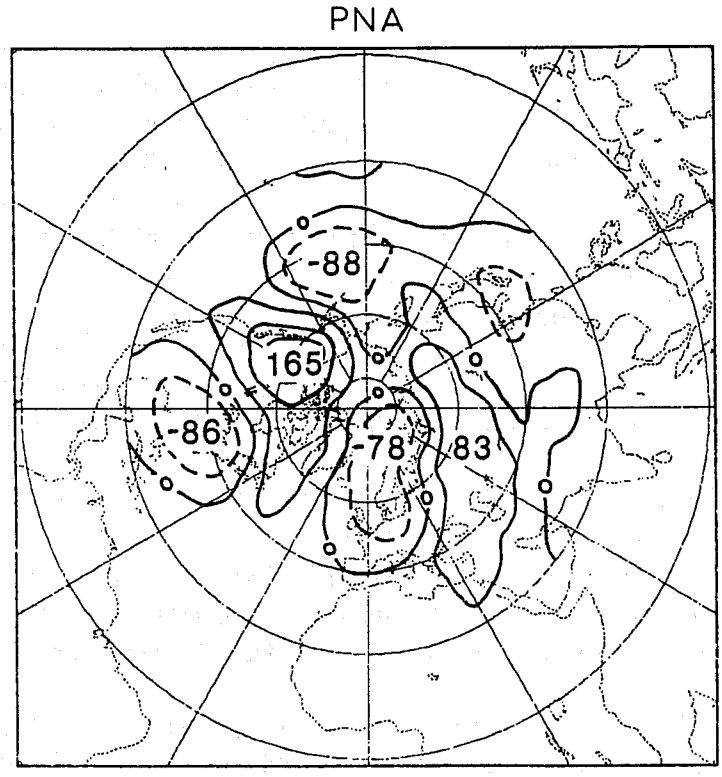

Figure 6.3: 1000-500hPa thickness anomalies associated with the PNA 500hPa height teleconnection pattern; for winter months only. From Gutzler *et al* (1988).

However, this does not imply that the observed surface warming is not associated with increases in CO_2. To see this, consider first a more parochial argument. If it is anomalously warm over London, then the chances are that the winds have a more southerly than normal component. If it is persistently warmer over London then the chances are the winds are persistently more southerly. This may or may not be due to enhanced CO_2. However, if one wants to know whether the fact that London is warmer is due to enhanced CO_2 then one must ask whether enhanced CO_2 will cause the wind to be more southerly.

Hence, similar to the 'London' argument, if one wants to know whether the fact that the hemispheric mean temperature anomaly has been persistently positive is due to enhanced CO_2, then one should ask whether enhanced CO_2 will increase the probability of the regimes in Fig 3.7a,c being observed. The question then arises; how could such an increase in the PDF of these regimes be most effectively achieved? Certainly, the adjoint analysis that we have discussed in this paper suggests that the most effective way to force an increase in the frequency of a regime is not achieved by a forcing which projects directly on the regime's geographical structure.

Precisely this question arose in section 4.2 in trying to understand what processes model systematic error was most sensitive to. One way to study this is through the sensitivity analysis described in section 3.5. We can imagine taking an atmospheric model trajectory over, let's say, a decade. For every trajectory segment say of order 10 days or so, we can compute the sensitivity of the positive PNA regime by integrating the regime backwards with the adjoint model. Each trajectory segment will have its own sensitivity pattern. By compositing over many different trajectory segments we get a mean sensitivity for the regime of interest.

Such a calculation is currently in progress (Susanna Corti, personal communication).

However, the adjoint eigenmode results shown in Fig 4.4 already gives us an approximate idea of the difference between the sensitivity structure and the regime structure. In particular, Fig 4.4 suggests that extratropical quasi-stationary Rossby wave patterns are likely to be sensitive to forcing in the Indonesian area. This result is consistent with the SST anomaly experiment shown in Fig 4.5, where a localised SST anomaly of about 1K could induce a substantial extratropical response, not altogether different from the positive PNA regime patterns shown in Fig 3.7.

Hence, even though we might only be interested in anthropogenic changes in hemispheric mean temperature, the large-scale (nonlinear) dynamics of the atmosphere appear to lead us to focus attention onto the possible impact of enhanced CO_2 on key physical processes in specific localised sensitive regions of the globe; the very antithesis of the global greenhouse effect.

It can be noted that in fact SSTs have increased over the west Pacific and Indian Ocean over the last few decades. Fig 6.4a (from Latif *et al*, 1996) shows the linear trend in SST (deg C/yr) over the period 1949-1991, Fig 6.4b shows the percentage of variance that this linear trend explains. It can be seen that the trend over the West Pacific and the Indian Ocean explains a relatively large part of the observed variance in SST in those areas.

Now what has this discussion to do with the predictability of climate change? According to these ideas, if we are to be able to simulate accurately the global atmospheric response to enhanced CO_2, it may be necessary to simulate very accurately how CO_2 influences the atmosphere in very specific regions of the globe (specifically over the warm pool area), and perhaps less accurately elsewhere. At present, uncertainties in basic radiative flux parametrisations in the warm pool area certainly exceed the basic $4W/m^2$ associated with radiative effect of doubled CO_2.

Despite these remarks, the predictability of climate change may be greater in the northern summer. In summer, the role of regime dynamics may be weakest, and the radiative greenhouse mechanism may be most significant. Moreover, according to the results of Wallace *et al* (1996) the amorphous component of hemispheric temperature change has its largest amplitude in summer.

Let us conclude this section by asking why the IPCC GCM simulations have not replicated the Angell observations? It is possible that the large-scale dynamics of many GCMs is still inadequate, and that the simulated warming in the 300-100hPa region is a manifestation of this inadequacy. For example, stationary-wave amplitudes in many GCMs are still poor, although recent diagnoses have suggested that weather regime structure does exist in the latest generation of atmospheric climate models (Haines and Hannachi, 1995). My guess is that as models improve, particularly in their representation of low-frequency atmospheric variability, the vertical structure of the response of GCMs to observed CO_2 will correspond more and more closely to the observed vertical structure of warming. (Of course I am aware that there are other complicating factors in discussing these issues, related to the observed depletion of ozone and enhancement in sulphate aerosols.)

7 Unification and rationalisation of climate and weather prediction models.

In this paper the notion of predictability has been reviewed, incompletely, on timescales of days, seasons and decades. In doing so we have used both simple and comprehensive models. Simple models are useful in order to formulate hypotheses and to study basic

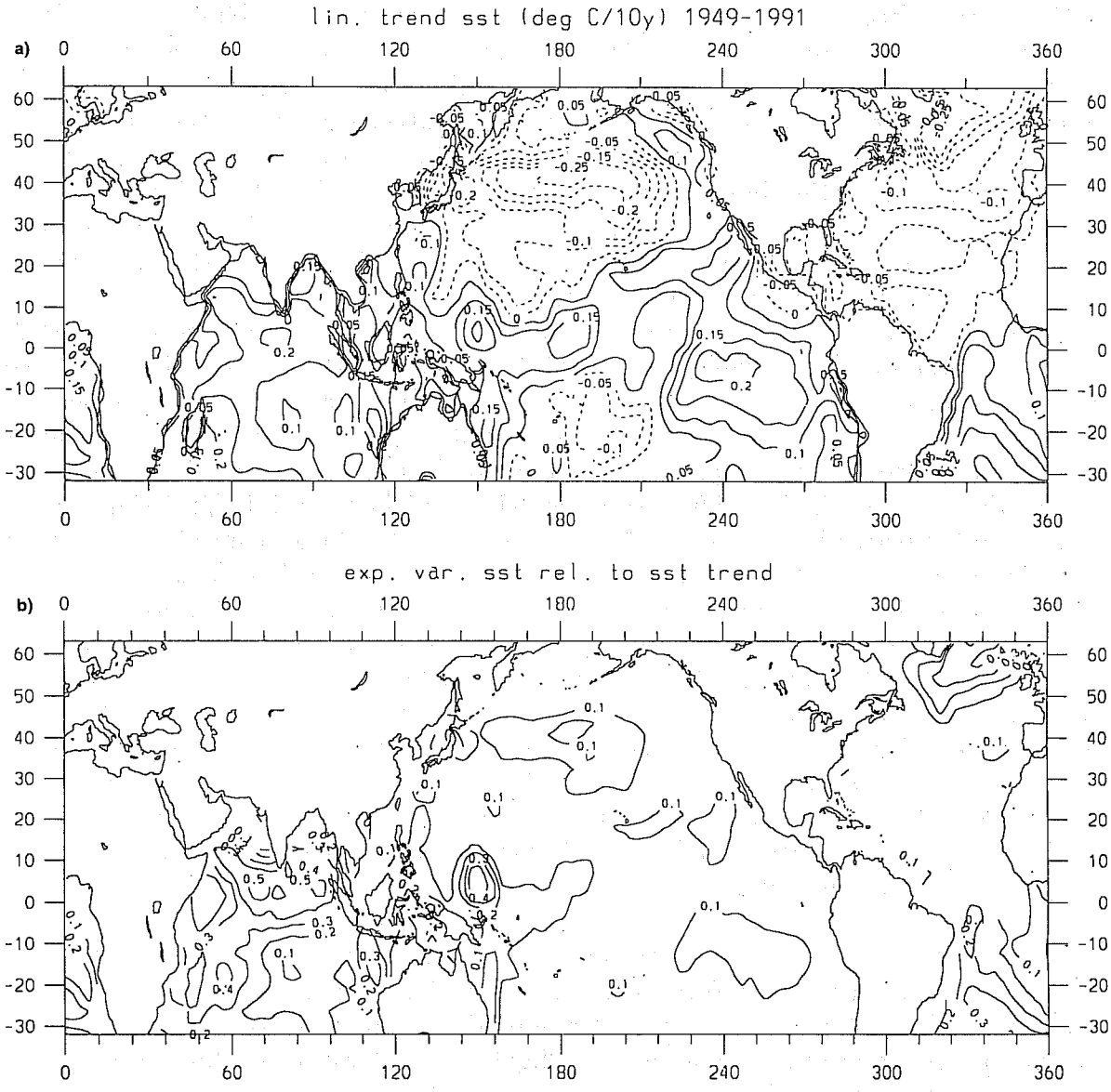

Figure 6.4: Spatial distribution of linear trend coefficients of observed SST (degrees C/ decade) for the period 1949-1991. b) Variances explained in SST by the linear trends. From Latif, *et al* (1996).

mechanisms, but quantitative assessment of predictability can only be achieved with comprehensive model studies. On timescales of days, the comprehensive models were based on those used for numerical weather prediction; on timescales of decades, global climate models were clearly most appropriate.

One of the successes of our subject in recent years has been the blurring of divisions between these two classes of model. Models that were primarily developed as weather prediction models are now used for climate prediction. Indeed some institutes develop unified models which are used for both climate and weather forecasting in equal measure.

At ECMWF, I have long taken the view that if a weather prediction model is to be successful in predicting blocking activity, for example, it should be able to simulate blocking activity satisfactorily in terms of its own climate. Similarly, it would seem reasonable to expect that a coupled model used for forecasting El Niño should be able to simulate El Niño variability in climate mode.

However, the converse is also true. As IPCC (1990) state, '..confidence in a model used for climate simulation will be increased if the same model is successful when used in a forecasting mode'. This conclusion is consistent with the analysis of the climate predictability problem in section 7, where it was suggested that in order that climate change be predictable, errors in flux representation must be locally less than 4 W/m^2 in regions such as the warm pool. Tolerable errors elsewhere might exceed $4W/m^2$ significantly. This moves the persective of climate change away from the global point of view, towards the local point of view. In my opinion, the best way to reduce these local flux errors is through comparison with detailed observations over the relevant area, *eg* from the TOGA COARE experiment (Webster and Lucas, 1992). However, such data are only made over limited periods of time, and therefore only cover specific synoptic situations. A comparison of COARE fluxes with some mean climatology from a long integration of a climate model is clearly inadequate. In comparing model with data, the model should be run in forecast mode. Short-range forecast errors in fluxes can then be compared directly with the observations, and the impact of revisions to the model physics (*eg* to cloud parametrisation schemes) can be readily validated. By validating the model for predictions of the first kind, we should have improved the model's reliability in making predictions of the second kind.

In addition to these concerns, we need to be able to pool modelling resources in order to test hypotheses in a fashion in which problems of model dependence can be minimised. The Atmospheric Model Intercomparison Project (Gates, 1993) is a good example of collaborative research that highlights the successes and limitations of the current generation of models.

However, it has been more difficult, on the basis of these intercomparison studies, to provide corrective prescriptions that will reduce the overall level of model bias. In my opinion, a fundamental question that the climate community needs to address, is whether we can achieve the required level of model accuracy for reliable climate prediction through the development of a diverse range of GCMs, maintained on an individual institute basis, or whether resources should be pooled into the detailed investigation and development of a smaller subset of proven models. I have my views (Palmer and Webster, 1995), I would like to hear yours!

Acknowledgements

I would like to thank Jan Barkmeijer, David Battisti, Roberto Buizza, Ying-Quei Chen, Ron Gelaro, David Rowell and Stephen Griffies for providing me with material which has yet to be published. I am also grateful to Andy Moore and David Stephenson

for very helpful comments on an earlier version of the manuscript.

References

ANGELL, J.K., 1988, Variations and trends in tropospheric and stratospheric global temperatures. 1958-87. *J.Clim.*, **1**, 1296-1313.

ABARBANEL, H.D.I., R.BROWN, AND M.B.KENNEL, 1991, 'Variation of Lyapunov exponents on a strange attractor', *Journal of Nonlinear Science*, **1**, 175-199.

BALMADEDA, M.A., M.K.DAVEY, AND D.L.T.ANDERSON, 1995, Decadal and seasonal dependence of ENSO prediction skill. *J.Climate.; In press.*

BARKMEIJER, J., P.HOUTEKAMER AND X.WANG, 1993, Validation of a skill prediction method. *Tellus*, **45A**, 424-434.

BATTISTI, D.S., 1988, Dynamics and thermodynamics of a warming event in a coupled tropical atmosphere-ocean model. *J Atmos Sci*, **45**, 2889-2919.

BJERKNES, J., 1964, Atlantic air-sea interaction. *Advances in Geophysics., Academic Press*, **10**, 1-82.

BLUMENTHAL, B., 1991, Predictability of a coupled ocean-atmosphere model. *J Climate*, **4**, 766-784.

BOUTTIER, F., 1993, The dynamics of error covariances in a barotropic model. *Tellus*, **45A**, 408-423.

BUIZZA, R. AND T.N.PALMER, 1995, The singular vector structure of the atmospheric general circulation. *J Atmos Sci.* **52**, 1434-1456.

BUIZZA, R., R. GELARO, F.MOLTENI AND T.N.PALMER, 1996, Predictability studies with high resolution singular vectors. *Q.J.R.Meteorol.Soc., submitted.*

CACUCI, D.G., 1981, Sensitivity theory for nonlinear systems: I: Nonlinear functional analysis approach. *J.Math.Phys.*, **22**, 2794-2802.

CANE, M.A., S.ZEBIAK, AND S.DOLAN, 1986, Experimental forecasts of El Niño. *Nature*, **321**, 827-832.

CHARNEY, J.G., 1947, The dynamics of long waves in a baroclinic westerly current. *J Meteor*, **4**, 135-163.

CHARNEY, J.G., AND J.SHUKLA, 1981, Predictability of monsoons. Monsoon Dynamics, *J.Lighthill and R. Pearce, Eds., Cambridge University Press, 735pp.*

CHEN, W.Y. AND H.M.VAN DEN DOOL, 1996, Asymmetric impact of ENSO on atmospheric internal variability over the north Pacific. *J.Clim. Submitted.*

CHEN, Y-Q., D.S.BATTISTI, T.N.PALMER, J.BARSUGLI AND E.S.SARACHIK, 1996, A study of the predictability of tropical Pacific SST in a coupled atmosphere/ocean model using singular vector analysis: the role of the annual cycle and the ENSO cycle. *Mon. Wea. Rev. Submitted.*

CHENG, X., AND J.M.WALLACE, 1993, Cluster analysis of the northern hemisphere wintertime 500-hPa height field: spatial patterns. *J. Atmos. Sci.*, **50**, 2674-2696.

CORTI, S., 1994, Modellistica dei regimi di circolazione atmosferica alle medie latitudini durante la stagione invernale. *PhD thesis. Available from University of Bologna, Physics Department. pp233.*

COURTIER, P, C.FREYDIER, J-F.GELEYN, F.RABIER, AND M.ROCHAS, 1991, The Arpege project at Mto-France. Proceedings of ECMWF Seminar on 'Numerical methods in atmospheric models', Shinfield Park, Reading RG2 9AX, UK, 9-13 September 1991, 2, *193-231.*

DALY, A.W., 1978, The response of North Atlantic sea surface temperature to atmospheric forcing processes. *Q.J.R.Meteorol.Soc.*, **104**, 363-382.

DALEY, R., 1991, Atmospheric data analysis. *Cambridge University Press. 457pp.*

DIX, M.R., AND B.G.HUNT, 1995, Chaotic influences and the problem of deterministic seasonal predictions. *Int. J. Climatol.*, **15**, 729-752.

DOLE, R.M. AND N.D.GORDON, 1983, Persistent anomalies of the Northern Hemisphere wintertime circulation: Geographical distribution and regional persistence characteristics. *Mon.Wea.Rev.*, **106**, 746-751.

EADY, E.T., 1949, Long waves and cyclone waves. *Tellus*, **1**, 33-52.

FARRELL, B.F., 1989, Optimal excitation of baroclinic waves. *J Atmos Sci*, **46**, 1193-1206.

FARRELL, B.F., 1990, Small error dynamics and the predictability of atmospheric flows. *J.Atmos.Sci.*, **47**, 2409-2416.

FARRELL, B.F. AND P.J.IOANNOU, 1996, Generalised stability theory. Part I: Autonomous operators. *J.Atmos.Sci., submitted.*

FISHER, M. AND P.COURTIER, 1995, Estimating the covariance matrices of analysis and forecast error in variational data assimilation. *ECMWF Technical Memorandum, 220.*

FOLLAND, C.K. AND D.P.ROWELL, 1995, Workshop on simulations of the climate of the twentieth century using GISST. Climate Research Technical Note 56. Hadley Centre. Meteorological Office. Bracknell UK. pp 111

GATES, W.L., 1993, AMIP: The Atmospheric Model Intercomparison Project. *Bull. Amer. Meteor. Soc.*, **73**, 1962-1970.

GILL, A.E., 1980, Some simple solutions for heat-induced tropical circulation. *Q J R Met Soc*, **106**, 447-462.

GRIFFIES, S.M. AND K.BRYAN, 1996, North Atlantic thermohaline circulation predictability in a coupled ocean-atmosphere model. *J.Climate. In press.*

GUTZLER, D.S., R.D.ROSEN, AND D.A.SALSTEIN, 1988, Patterns of interannual variability in the northern hemisphere wintertime 850mb temperature field. *J.Clim.*, **1**, 949-964.

HAINES, K. AND A.HANNACHI, 1995, Weather regimes in the Pacific from a GCM. *J.Atmos.Sci.*, **52**, 2444-2462.

HANSEN, A.R. AND A.SUTERA, 1986, On the probability density distribution of the planetary-scale atmospheric wave amplitude. *J.Atmos.Sci.*, **43**, 3250-3265.

HANSEN, A.R. AND A.SUTERA, 1995, Large amplitude flow anomalies in northern hemisphere midlatitudes. *J. Atmos. Sci*, **52**, 2133-2151

HARTMANN, D.L., R.BUIZZA, AND T.N.PALMER, 1995, Singular vectors: the effect of spatial scale on linear growth of disturbances, *J. Atmos. Sci.*, **52**, 3885 3894.

HASSELMANN, K., 1976, Stochastic climate models. Part I: Theory. *Tellus*, **28**, 473-485.

HELD, I.M. AND P.J.PHILLIPPS, 1993, Sensitivity of the eddy momentum flux to meridional resolution in atmospheric GCMs. *J. Climate*, **6**, 499-507.

HESS, P. AND H.BREZOWSKY, 1977. Katalog der Grosswetterlagen, *Ber. Dtsch. Wetterdienst, Offenbach*, **113**, Bd 15, 39pp.

HOLLINGSWORTH, A., 1987, Objective analysis for numerical weather prediction. In: Short and Medium Range Numerical Weather Prediction. Collected papers presented at WMO/IUGG NWP symposium , Tokyo, 4-8 August, 1986, ed by T.Matsuno, *Special Volume of the J.Meteor.Soc.Japan.* **11**, 59.

HOSKINS, B.J., M.E.MCINTYRE AND A.W.ROBERTSON, 1985, On the use and significance of isentropic potential vorticity maps. *Q.J.R.Meteorol. Soc.*, **111**, 877-946.

IPCC, (INTERGOVERNMENTAL PANEL ON CLIMATE CHANGE) 1990, Climate Change: the IPCC Scientific Assessment, J.T.Houghton, G.J.Jenkins and J.J.Ephraums (eds). *Cambridge University Press, Cambridge, UK, 198pp.*

IPCC, 1992, Climate change, the supplementary report to the IPCC scientific assessment, J.T. Houghton, B.A.Callander and S.K.Varney (eds). *Cambridge University Press, Cambridge, UK, 365pp.*

JAMES, I.N. AND P.M.JAMES, 1989, Ultra-low-frequency variability in a simple atmospheric model. *Nature,* **342,** 53-55.

KIMOTO, M. AND M.GHIL, 1993, Multiple flow regimes in the northern hemisphere winter. Part I: Methodology and hemispheric regimes. *J. Atmos. Sci.,* **50,** 2625-2643.

LATIF, M. AND T.P.BARNETT, 1994, Causes of decadal climate variability over the North Pacific and North America. *Science,* **266,** 634-637.

LATIF, M., R.KLEEMAN AND C.ECKERT, 1996, Greenhouse warming, decadal variability, or El Niño? An attempt to understand the anomalous 1990s. *J.Clim. Submitted.*

LILLY, D.K., 1983, Stratified turbulence and the mesoscale variability of the atmosphere. *J.Atmos.Sci.,* **40,** 749-761.

LINDZEN, R.S., 1988, Instability of plane parallel shear flow (towards a mechanistic picture of how it works). *PAGEOPH,* **126,** 103-121.

LORENZ, E.N., 1963A, Deterministic nonperiodic flow. *J Atmos Sci,* **20,** 130-141.

LORENZ, E.N., 1963B, The predictability of hydrodynamic flow. *Trans New York Acad Sci, Ser 2,* **25,** 409-432.

LORENZ, E.N., 1965, A study of the predictability of a 28-variable atmospheric model. *Tellus,* **17,** 321-333.

LORENZ, E.N., 1975, Climate predictability: The physical basis of climate modelling. *WMO, GARP Pub.Ser.,* **16,** 132-136.

MANABE, S. AND R.J.STOUFFER, 1996, Low-frequency variability of surface air-temperature in a 1000 Year integration of a coupled ocean-atmosphere model. *J.Clim. To appear.*

MANSFIELD, D.A., 1993, The storm of 10 January 1993. *Met Mag,* **122,** 140-146.

MARCHUK, G.I., 1974, Osnovnye i soprazhennye uravneniya dinamiki atmosfery i okeana. *Meteor. Gidrol.,* **2,** 9-37.

MARDIA, K,V., J.T.KENT, AND J.M.BIBBY, 1979, Multivariate Analysis. *Academic Press, London. 518pp.*

MARSHALL, J. AND F.MOLTENI, 1993, Toward a dynamical understanding of planetary-scale flow regimes. *J Atmos Sci,* **50,** 1792-1818.

METAIS, O., J.J.RILEY, AND M.LESIEUR, 1994, Numerical simulations of stably-stratified rotating turbulence. From 'Stably stratified flow and dispersion over topography.' Eds I.P. Castro and N.J.Rockliff. *Clarendon Press. Oxford.*

MO, K.C. AND M.GHIL, 1988, Cluster analysis of multiple planetary flow regimes. *J. Geophys. Res., 93D,* **10,** 927-10 952.

MOLTENI, F., S.TIBALDI AND T.N.PALMER, 1990, Regimes in the wintertime circulation over northern extratropics I: Observational evidence. *Q.J.R.Meteor.Soc.,* **116,** 31-67.

MOLTENI, F. AND S.TIBALDI, 1990, Regimes in the wintertime circulation over northern extratropics. II: Consequences for dynamical predictability. *Q.J.R.Meteor.Soc.,* **116,** 1263- 1288.

MOLTENI, F. AND T.N.PALMER, 1993, Predictability and finite-time instability of the northern winter circulation. *Q J R Met Soc,* **119,** 269-298.

MOLTENI, F., R.BUIZZA, T.N.PALMER, AND T.PETROLIAGIS, 1996, The ECMWF ensemble prediction system: methodology and validation. *Q.J.R. Meteorol. Soc.,* **122,** 73-120.

MOORE, A.M. AND R.KLEEMAN, 1996, The dynamics of error growth and predictability in a coupled model of ENSO. *Q.J.R.Meteorol.Soc., submitted.*

MUKOUGAWA, H., M.KIMOTO, AND S.YODEN, 1991, A relationship between local error growth and quasi-stationary states in the Lorenz system. *J Atmos Sci,* **48,** 1231-1237.

MÜNNICH, M., M.A.CANE, AND S.E.ZEBIAK, 1991, A study of self-excited oscillations in a tropical ocean-atmosphere system. Part II: Nonlinear cases. *J Atmos Sci,* **48,** 1238-1248.

NOBLE, B. AND J.W.DANIEL, 1977, Applied Linear Algebra. *Prentice-Hall Inc. 477 pp.*

ORR, W.M.F., 1907, The stability or instability of the steady motions of a perfect liquid and of a viscous liquid,. *Proc. Roy. Irish Acad.,* **A27,** 9-138.

OSELEDEC, V.I., 1968, A multiplicative ergodic theorem. Lyapunov characteristic numbers for dynamical systems. *Trudy Mosk Mat Obsc,* **19,** 197.

PALMER, T.N., 1993, Extended-range atmospheric prediction and the Lorenz model. *Bull Am Met Soc,* **74,** 49-65.

PALMER, T.N., 1988, Medium and extended-range predictability and stability of the Pacific/North American mode. *Q.J.R.Meteor.Soc.,* **114,** 691-713.

PALMER, T.N., 1993, A nonlinear dynamical perspective on climate change. *Weather,* **48,** 313-348.

PALMER, T.N., 1994, Chaos and predictability in forecasting the monsoons. *Proc.Indian Natn. Sci. Acad.,* **60A,** 57-66.

PALMER, T.N., AND D.A.MANSFIELD, 1986, A study of wintertime circulation anomalies during past El Niño events using a high resolution general circulation model. II: Variability of the seasonal mean response. *Q.J.R.Meteor.Soc.,* **112,** 639-660.

PALMER, T.N. AND Z.SUN, 1985. A modelling and observational study of the relationship between sea surface temperatures in the northwest Atlantic and the atmospheric general circulation. *Q.J.R.Meteor.Soc.,* **111,** 691-713.

PALMER, T.N., R.BUIZZA, F.MOLTENI, Y-Q.CHEN AND S.CORTI, 1994, Singular vectors and the predictability of weather and climate. *Phil.Trans.R.Soc.Lond.A,* **348,** 459-475.

PALMER, T.N. AND P.J.WEBSTER, 1995, Towards a unified approach to climate and weather prediction. Global change. Proceedings of the first Demetra meeting held at Chianciano Terme, Italy. Published by the European Commission. *EUR 15158 EN. 429pp.*

RABIER, F., E.KLINKER, P.COURTIER, AND A.HOLLINGSWORTH, 1996, Sensitivity of two-day forecast errors over the northern hemisphere to initial conditions. *Q.J.R. Meteor.Soc.,* **122,** 121-150.

RATCLIFFE, R.A.S. AND R.MURRAY, 1985, New lag associations between North Atlantic sea temperatures in the north-west Atlantic and the atmospheric general circulation. *Q.J.R.Meteorol.Soc.,* **96,** 226-246.

SARACHIK, E.S., 1990, Predictability of ENSO. In 'Climate-Ocean Interaction' ed M.E.Schlesinger, *Kluwer Academic Publishers. Dordrecht, the Netherlands. pp385.*

SIMMONS, A.J., D.M.BURRIDGE, M.JARRAUD, C.GIRARD, AND W.WERGEN, 1989, The ECMWF Medium-Range Prediction Models Development of the Numerical Formulations and the Impact of Increased Resolution. *Meteorol Atmos Phys,* **40,** 28-60.

SLEIJPEN AND VAN DER VORST, 1995, A Jacobi-Davidson iteration method for linear eigenvalue problems. *Universiteit Utrecht, Department of Mathematics, preprint 856.*

SPENCER, R.W., AND J.R.CHRISTY, 1990, Precise monitoring of global temperature trends from satellites. *Science,* **247,** 1558-1562.

SPERBER, K.R. AND T.N.PALMER, 1996, Interannnual tropical rainfall variability in general circulation model simulations associated with the atmospheric model intercomparison project. *J.Clim. submitted.*

STRANG, G., 1986, Introduction to applied mathematics. *Wellesley-Cambridge press, 758 pp.*

THOMPSON, J.M.T. AND H.B.STEWART, 1991, Nonlinear dynamics and chaos. *John Wiley. Chichester. pp376*

TOTH, Z., 1992, Quasi-stationary and transient periods in the Northern Hemisphere winter. *Mon.Wea. Rev.,* **119,** 1602-1611.

TOTH, Z. AND E.KALNAY, 1993, Ensemble forecasting at NMC: The generation of perturbations. *Bull. Amer. Meteor. Soc.*, **74,** 2317-2330.

TOTH, Z. AND E.KALNAY, 1996, Ensemble forecasting at NMC and the breeding method. *Monthly Weather Review. Submitted.*

TREVISAN, A., 1993, Impact of transient error growth on global average predictability measures. *J Atmos Sci,* **50,** 1016-1028.

VON STORCH, H., 1988, A statistical comparison with observations of control and El Niño simulations using the NCAR CCM. *Beitrge sur Physik der Atmosphre,* **60,** 464-477.

WALLACE, J.M. AND D.S.GUTZLER, 1981, Teleconnections in the geopotential height field during the northern hemisphere winter. *Mon Wea.Rev.,* **109,** 784-812.

WALLACE, J.M., X.CHENG AND D.SUN, 1991, Does low-frequency atmospheric variability exhibit regime-like behaviour? *Tellus,* **43AB,** 16-26.

WALLACE, J.M., Y.ZHANG AND J.A.RENWICK, 1996, Dynamically-induced variability in hemispheric mean surface air temperature. *Science. To appear.*

WEBSTER, P.J., 1995, The annual cycle and the predictability of the tropical coupled ocean-atmosphere system, *Meteor. and Atmos. Phys.,* **56,** 33-35.

WEBSTER, P.J. AND R.LUCAS, 1992, TOGA-COARE: The Coupled Ocean-Atmosphere Response Experiment. *Bull. Amer. Meteor. Soc.,* **73,** 1377-1416.

XUE, Y., M.A.CANE, S.E.ZEBIAK AND M.B.BLUMENTHAL, 1994, On the prediction of ENSO. A study with a low order Markov. *Tellus,* **46,** 512-528.

YANG, S. AND B.REINHOLD, 1991, How does low-frequency variance vary? *Mon.Wea.Rev.,* 119-127.

ZEBIAK, S.E. AND M.A.CANE, 1987, A model El Niño - Southern Oscillation. *Mon Wea Rev,* **115,** 2262-2278.

ZHANG, Z., 1988, The linear study of zonally asymmetric barotropic flows. *PhD Thesis. University of Reading, UK.*